


# Proximity spin-orbit and exchange coupling in ABA and ABC trilayer graphene van der Waals heterostructures

Klaus Zollner<sup>1,\*</sup>, Martin Gmitra<sup>2</sup>, and Jaroslav Fabian<sup>1</sup>

<sup>1</sup>*Institute for Theoretical Physics, University of Regensburg, 93053 Regensburg, Germany*

<sup>2</sup>*Institute of Physics, Pavol Jozef Šafárik University in Košice, 04001 Košice, Slovakia*

 (Received 7 January 2022; revised 24 February 2022; accepted 3 March 2022; published 21 March 2022)

We investigate the proximity spin-orbit and exchange couplings in ABA and ABC trilayer graphene encapsulated within monolayers of semiconducting transition-metal dichalcogenides and the ferromagnetic semiconductor  $\text{Cr}_2\text{Ge}_2\text{Te}_6$ . Employing first-principles calculations, we obtain the electronic structures of the multilayer stacks and extract the relevant proximity-induced orbital and spin interaction parameters by fitting the low-energy bands to model Hamiltonians. We also demonstrate the tunability of the proximity effects by a transverse electric field. Using the model Hamiltonians, we also study mixed spin-orbit/exchange coupling encapsulation, which allows us to tailor the spin interactions very efficiently by the applied field. We also summarize the spin-orbit physics of bare ABA, ABC, and ABB trilayers, and we provide—along with the first-principles results of the electronic band structures, density of states, spin splittings, and electric-field tunabilities of the bands—a qualitative understanding of the observed behavior and realistic model parameters as a resource for model simulations of transport and correlation physics in trilayer graphene.

DOI: [10.1103/PhysRevB.105.115126](https://doi.org/10.1103/PhysRevB.105.115126)

## I. INTRODUCTION

Two-dimensional (2D) van der Waals (vdW) materials are vital building blocks in the design of ultracompact electronic and spintronic devices [1–5]. In this context, proximity-induced phenomena [6,7] were found to be of great importance, since 2D materials influence each other's electronic and spin properties in vdW heterostructures. Recently, it has been demonstrated that superconductivity [8–10], magnetism [11–23], and spin-orbit coupling (SOC) [24–33] can be induced on demand in such weakly glued vdW multilayers. In addition, gating, twisting, stacking, and straining are efficient tunability knobs to tailor these spin interactions [13,28,30,34–41], while the individual materials also preserve a great degree of autonomy.

In twisted vdW heterostructures [42–45], the interlayer interaction can be controlled by the twist angle. In this context, bilayer graphene (BLG) was the first model playground for gate- and twist-tunable correlated physics [44,46–51], as well as for layer-dependent proximity-induced spin interactions [12,52–60]. At very small twist angles ( $\approx 1^\circ$ ), a sharp peak arises in the density of states (DOS) of twisted BLG, which is associated with flat bands [61] in the dispersion. By doping the twisted BLG, it can become insulating, ferromagnetic [51], or superconducting [46–50,62,63]. As a logical next step, also twisted BLG-BLG structures were considered [64–67], where the flat bands are additionally tunable by a gate field.

In addition, recent experiments [55] could demonstrate that the proximity-induced Rashba and valley Zeeman SOC in twisted-BLG/ $\text{WSe}_2$  heterostructures induce orbital mag-

netism without the need for a rotational alignment to a hexagonal boron-nitride substrate [51,68]. Moreover, the transition-metal dichalcogenide (TMDC)  $\text{WSe}_2$  can help to stabilize superconductivity in twisted BLG [48], emphasizing the role of the dielectric environment. For the interpretation of such experimental results, it is also important to have qualitative and quantitative knowledge about the proximity effects in TMDC/BLG heterostructures [60].

Unlike mono- and bilayer graphene, trilayer graphene (TLG) has not yet been systematically investigated for spin proximity effects. The spin-orbit physics of pristine TLG in ABA and ABC stackings was investigated by *ab initio* calculations [69] and tight-binding modeling [70], revealing many subtleties of the low-energy bands stemming from the presence of *d*-orbitals which give rise to spin-orbit splittings on the order of  $10 \mu\text{eV}$ . Depending on the stacking order of the three layers, either ABA or ABC, very different electronic structures can be realized with distinct features in electronic and spin transport [71,72] and gate-tunable SOC [73]. TLG is also important from the topological perspective, since the ABC structure potentially hosts quantum spin Hall and quantum valley Hall states [74], while there is evidence for a giant topological magnetic moment in ABA TLG [75]. Also interesting is the energetics of the different stackings; see, for example, Ref. [76].

More recently, TLG has emerged as a novel platform for correlated electrons [77–83], as there is one more independent layer, leading to a wider range of magic angles. As a consequence, the tunability of the electronic and superconducting properties is superior to that in BLG, as recently demonstrated [78,84–87] and theoretically explained [88]. Remarkably, a zero-field superconducting diode, signaling an interplay of spin-orbit physics and time-reversal symmetry-broken phase, has been demonstrated in twisted-TLG/ $\text{WSe}_2$

\*klaus.zollner@physik.uni-regensburg.de

heterostructures [89–91]. For the interpretation and quantitative theoretical understanding of such experiments, it is important to have a deeper microscopic knowledge of the spin proximity effects in TLG. Providing such a resource is the goal of our manuscript.

In particular, we investigate, by performing first-principles calculations, the electronic structures of ABA and ABC TLG encapsulated within strong SOC semiconductors  $\text{MoSe}_2$  and  $\text{WSe}_2$  and ferromagnetic monolayers  $\text{Cr}_2\text{Ge}_2\text{Te}_6$  (CGT). We provide the essential band-structure information, low-energy band dispersions, spin splittings of the low-energy bands, spin textures, and the behavior of the Dirac bands in the presence of a transverse electric field. To provide a reference for the encapsulated systems, we summarize the essential low-energy physics of bare ABA and ABC TLG, also including ABB TLG for completeness. While pristine graphene exhibits intrinsic SOC of  $10\text{--}20\text{ }\mu\text{eV}$ , encapsulated TLG displays spin splittings of some meV, strongly tunable by the electric field.

In terms of modeling, we focus on the proximity-induced spin-orbit and exchange couplings, and we demonstrate that in order to reproduce the density functional theory (DFT) data, it is sufficient to modify only the spin interactions of the outer layers of encapsulated TLG. The effective low-energy Hamiltonians, which are fitted to the TLG dispersions to obtain reasonable parameter sets, nicely reproduce the first-principles data. Moreover, we show that the model reproduces the data also in the presence of a transverse electric field, whereby modifying only a few effective couplings is sufficient for a quantitative comparison.

Employing the model, with fitted proximity spin-orbit and exchange couplings separately, we then provide predictions for ex-so-tic heterostructures [54,92] which comprise both a strong SOC monolayer and a ferromagnetic monolayer, encapsulating ABA and ABC TLG. The interplay between spin-orbit and exchange coupling is imprinted onto the corresponding low-energy band structures and most markedly pronounced by the different band dispersions at  $K$  and  $K'$ . We also show that the band dispersions respond sensitively to the applied electric field, which can serve as a knob to change the spin polarization of the low-energy states in ABC TLG.

In all the studied cases, we provide both a qualitative understanding, based on the atomic arrangement and hybridization across the layers, and quantitative modeling with realistic parameters fitted to the DFT results, which should be useful for model simulations of TLG.

The paper is organized as follows: In Sec. II, we first discuss the electronic properties of bare TLG with ABA, ABC, and ABB stackings, under the influence of SOC and an external electric field, to have reference results for the encapsulated structures. In Sec. III, we present the encapsulated TLG geometries, address the structural setup, and summarize the calculation details for obtaining the electronic structures. In Sec. IV, we introduce the model Hamiltonians that capture the low-energy physics of encapsulated TLG (including orbital, SOC, and exchange terms), which are used to fit the DFT-calculated dispersions. In Sec. V, we then show and discuss the DFT-calculated electronic structures, along with the model Hamiltonian fits, of TMDC and CGT encapsulated TLG. In Sec. VI, we turn to the electric field tunability of the relevant low-energy bands of TMDC encapsulated TLG.

In Sec. VII, we discuss the interplay of spin interactions in CGT/TLG/TMDC heterostructures, on the model level, based on our results for TMDC and CGT encapsulated TLG. Finally, in Sec. VIII we conclude the manuscript.

## II. BARE TRILAYER GRAPHENE

Recent investigations on twisted-graphene/BLG heterostructures, which contain all three high-symmetry TLG stacking types (ABA, ABC, and ABB), reveal highly interesting topological properties [83,93–95]. For example, in Ref. [83] the electrical control of magnetism, which arises due to strong correlations by twisting graphene on top of BLG, has been demonstrated.

To obtain reference results for evaluating the proximity effects in encapsulated graphene trilayers, we briefly review the essential electronic properties of bare ABA, ABC, and ABB stackings, focusing on the energy dispersions of the lowest energy bands and the spin-orbit splittings. The electronic band structures of the bare trilayers were obtained by performing first-principles calculations employing a full potential linearized augmented plane wave (FLAPW) code based on density functional theory (DFT), as implemented in WIEN2K [96]. This code was already used to calculate SOC in monolayer and bilayer graphene [97–99], yielding results consistent with recent experimental findings [100,101].

In our implementation, exchange-correlation effects are treated with the generalized-gradient approximation (GGA) [102], including the DFT-D3 vdW dispersion correction [103]. We used a very dense  $k$ -point grid of  $120 \times 120 \times 1$  to accurately determine the Fermi level. The muffin-tin radius of carbon atoms is  $R_C = 1.34$  and the plane-wave cutoff parameter  $RK_{\text{MAX}} = 9.5$ . For all TLG stackings, we use the lattice parameter of bare graphene  $a = 2.46\text{ }\text{\AA}$ , with fixed interlayer distances of  $d = 3.3\text{ }\text{\AA}$ . To avoid interactions between periodic images of our slab geometries, we add a vacuum of about  $20\text{ }\text{\AA}$  in the  $z$  direction. An earlier account of WIEN2K TLG calculations can be found in Ref. [69], while multiorbital tight-binding modeling of ABC TLG in the presence of SOC was performed in Ref. [70].

### A. ABA

In Fig. 1 we show the lattice structure, the calculated energy dispersion, and a schematic energy level diagram for ABA TLG. Due to  $z$ -mirror symmetry, four nonequivalent atoms are present in the geometry; see Fig. 1(a). The low-energy band structure [see Fig. 1(b)] shows graphenelike Dirac states, as well as BLG-like parabolic bands, consistent with the literature [104–107]. The Dirac bands are exclusively formed by orbitals of the atoms in the outermost graphene layers. In contrast, the parabolic bands are formed by atoms  $B_1$ ,  $A_2$ , and  $B_3$ , which form nondimer interlayer pairs.

Without SOC, the bands remain spin-degenerate; see the scheme in Fig. 1(c). Including SOC, the degeneracy is lifted due to the absence of space-inversion symmetry, and the low-energy bands are split by about  $20\text{ }\mu\text{eV}$  (corresponding to the intrinsic SOC of pristine graphene monolayers [97]). The high-energy states—not shown in Fig. 1(b) but included in the energy level diagram in Fig. 1(c)—which are formed by atoms

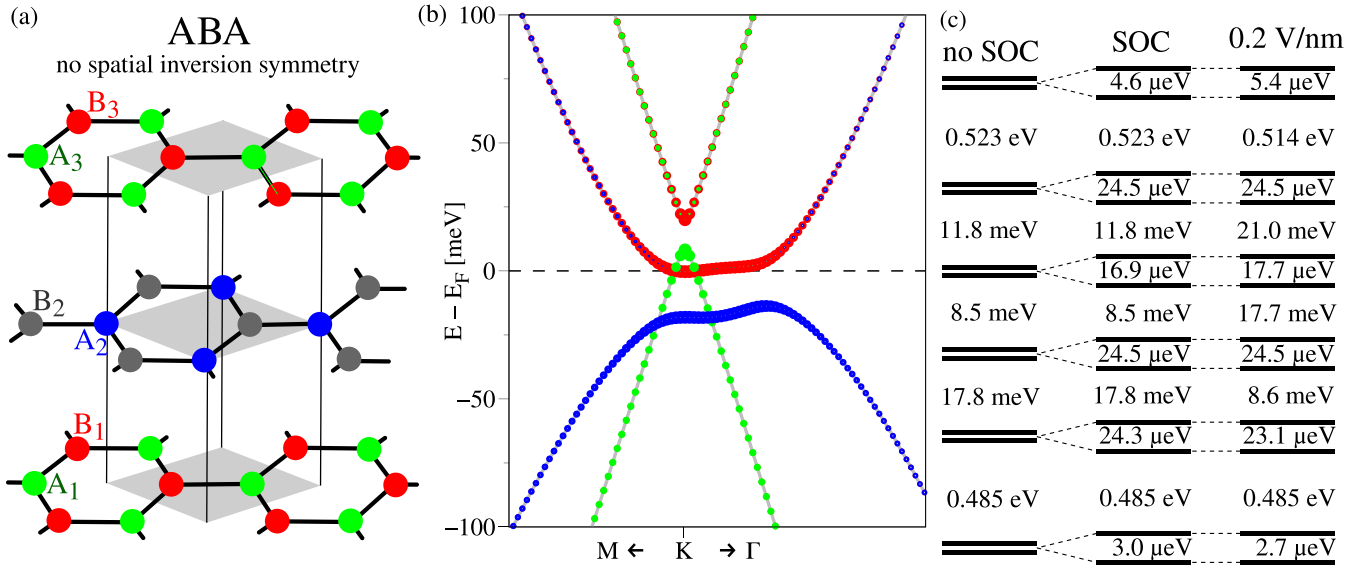


FIG. 1. (a) Lattice structure of the ABA TLG. Due to  $z$ -mirror symmetry, the sublattice atoms with the same color (red, blue, green, and gray) belong together. Gray rhombuses define the unit cells of the layers. (b) The DFT-calculated band structure in the vicinity of the  $K$  point. The bands are color-coded by their atomic projections as defined in (a). (c) The energy level diagram of states at the  $K$  point without SOC, with SOC, and with SOC in the presence of a perpendicular electric field of 0.2 V/nm.

$A_1$ ,  $B_2$ , and  $A_3$ , are about 500 meV away from the Dirac point at the Fermi level. The reason is that these atoms are coupled by direct interlayer hopping, pushing the corresponding bands away from the Fermi level, similar to bare BLG [99]. The spin-orbit splittings of the high-energy bands are just a few  $\mu\text{eV}$ . The diagram in Fig. 1(c) also indicates the effect of an applied transverse electric field that introduces a potential difference between the outermost layers. The field essentially reshuffles the energy levels, but mainly the band offsets of the Dirac and parabolic low-energy bands change, while the spin-

orbit splittings remain nearly unchanged for the electric field as large as 0.2 V/nm. In Appendix A, we show and discuss the evolution of the ABA TLG dispersion and DOS for electric fields up to 1 V/nm. We also provide model Hamiltonian fit results there, that nicely reproduce the dispersion.

### B. ABC

In Fig. 2 we show the lattice structure, the calculated energy dispersion, and an energy-level diagram for ABC

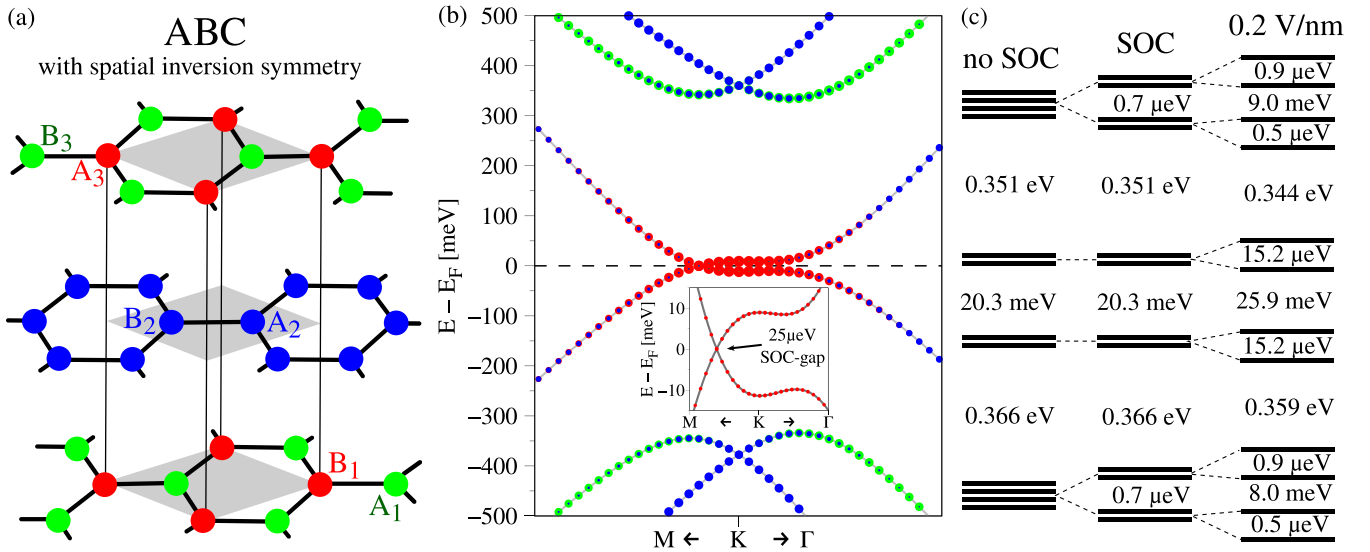


FIG. 2. (a) Lattice structure of the ABC TLG. Due to space inversion symmetry, the sublattice atoms of the same color (red, blue, and green) contribute equally to the energy bands. Gray rhombuses define the unit cells of the layers. (b) The DFT-calculated band structure in the vicinity of the  $K$  point. The bands are color-coded by their atomic projections as defined in (a). The inset in (b) shows a zoom to the low-energy bands near the Fermi level, indicating the conelike touching point, where a gap of about  $25 \mu\text{eV}$  arises due to SOC. (c) The energy level diagram of the low- and high-energy states at the  $K$  point without SOC, with SOC, and with SOC in the presence of a perpendicular electric field of 0.2 V/nm.

TLG. This structure has spatial inversion symmetry, and only three nonequivalent atoms are present in the geometry; see Fig. 2(a). From the band structure at the  $K$  point [see Fig. 2(b)], we find two flat low-energy bands that are formed by the outer-layer atoms  $B_1$  and  $A_3$ , although  $A_2$  and  $B_2$  become prominent at larger momenta away from  $K$ . The four high-energy bands, which are split off from the Fermi level by more than 0.35 eV, are built by sublattices  $A_1$ ,  $A_2$ ,  $B_2$ , and  $B_3$ . The presented dispersion is consistent with earlier reports [105,107–110].

At the  $K$  point, the low-energy bands are twofold spin degenerate, while the high-energy bands are even fourfold degenerate, in the absence of SOC; see Fig. 2(c). Due to spatial inversion symmetry, all bands remain spin degenerate, even when SOC is turned on. However, a tiny (about 0.7  $\mu$ eV) spin-orbit gap opens at the high-energy levels and removes the fourfold degeneracy. Zooming into the Fermi level, we find a conelike touching feature of the low-energy bands along the  $K \rightarrow M$  high-symmetry line; see Fig. 2(b). When SOC is included, the Dirac cones are split by 25  $\mu$ eV, which corresponds to the spin-orbit gap, caused almost solely by  $d$  orbitals of a pristine graphene monolayer [97].

When a perpendicular electric field is applied across the ABC TLG, the inversion symmetry, along with the spin degeneracy of the bands, gets lifted; see Fig. 2(c). The field introduces a potential difference between the outermost layers, leading to further gap openings in the spectrum. By increasing the field amplitude, the low-energy spin splittings at the  $K$  point first increase, then saturate at about 25  $\mu$ eV, and finally decrease again [69]. For a field of 0.2 V/nm, the splittings of the low-energy bands at the  $K$  point are about 15  $\mu$ eV; see Fig. 2(c). Near the Dirac cone vertex, the band splittings are 25  $\mu$ eV, again corresponding to the intrinsic SOC of monolayer graphene [97]. Such intrinsic splittings, which get exposed by an applied electric field and that do not depend on the field above some crossover value, are also present in BLG [99] and lead to a marked spin relaxation anisotropy, as already experimentally detected [111].

### C. ABB

In Fig. 3 we show the lattice structure, the calculated dispersion, and an energy level diagram for ABB TLG. Due to the absence of spatial inversion and  $z$ -mirror symmetry, all sublattice atoms are different; see Fig. 3(a). The band structure [see Fig. 3(c)] features parabolic high-energy bands at around 600 meV at the  $K$  point, predominantly formed by  $B_2$  atoms. The reason is that  $B_2$  is interlayer-coupled to both surrounding layers, splitting these states off to high energies. The low-energy bands near the  $K$  point are almost exclusively formed by  $B_1$ , with a small contribution from  $A_1$  and  $B_3$ . The reason is that  $B_1$  does not couple directly to the other layers, so the corresponding band remains close to the Dirac point. The intermediate bands are formed by  $A_2$  and  $A_3$  near the  $K$  point, because they are only connected by one interlayer coupling. The energy level diagram [see Fig. 3(b)] shows that the bands remain spin-degenerate without SOC. Including SOC lifts the degeneracy, because spatial inversion symmetry is absent. The low-energy valence (conduction) band is split by about 25  $\mu$ eV (8  $\mu$ eV). A transverse electric field

further opens the gap at the  $K$  point, while swapping the spin-orbit splittings—and the orbital composition of the bands themselves—of the low-energy valence and conduction bands (see also Fig. 18 in Appendix B). The high-energy bands remain nearly the same, except that band offsets are tunable by the field. In Appendix B we show the evolution of the ABB TLG dispersion and DOS for electric fields up to 1 V/nm. We also provide model Hamiltonian fit results there, which nicely reproduce the dispersion.

For the presented TLG dispersions, we have fixed all the interlayer distances to  $d = 3.3$  Å. In Appendix C, we compare the dispersions and DOS for ABA, ABC, and ABB TLG with relaxed interlayer distances. The ABB dispersion and DOS in particular are markedly modified, since the interlayer distances become highly asymmetric.

### D. Electric field effects

An important factor for correlation physics in TLG is the flatness of the dispersion, associated with van Hove singularities (VHS) in the DOS. Recently, superconductivity in ABC TLG was demonstrated [85], which is certainly strongly related with the electric field tunability of these VHS. Below we describe the electric tunability of ABC TLG, while in Appendixes A and B we show and discuss the electric field behavior of ABA and ABB TLG dispersions and their corresponding DOS.

In Fig. 4 we show the evolution of the dispersion and DOS for ABC TLG for electric fields up to 1 V/nm. The field opens a band gap at the Fermi level, since the low-energy bands are formed by atoms  $B_1$  and  $A_3$  (see Fig. 2) of the outermost graphene layers, now located in different potentials. Increasing the field up to 1 V/nm opens a sizable gap of about 90 meV in the spectrum. Also in the high-energy bands, gaps are introduced by the field. However, because they are split off in energy from the Fermi level, they are not so important for transport experiments. Viewing the corresponding DOS, we find VHS associated with the low-energy bands. As the electric field separates these bands in energy, they further flatten and the VHS become strongly pronounced.

Given the similarity of the electric field behavior of the low-energy bands of BLG [99] and ABC TLG, one can expect, for example, similar tunability of the valley  $g$ -factor as demonstrated for BLG [112,113]. Moreover, one can also expect a spin-orbit valve operation in ABC TLG, as experimentally and theoretically demonstrated in BLG/TMDC heterostructures [52,57].

In Fig. 4 we also compare DFT data and model Hamiltonian fits. Employing the parameters from Table III in Appendix A, we can perfectly fit the dispersions with applied electric field. The model Hamiltonian will be introduced in the following section when discussing encapsulated TLG heterostructures.

## III. ENCAPSULATED TRILAYER GRAPHENE

### A. Geometry setup

In the following, we focus on TLG in ABA and ABC stacking, which are of the most current interest. For both stacking types, we consider  $4 \times 4$  supercells of TLG to be encapsulated



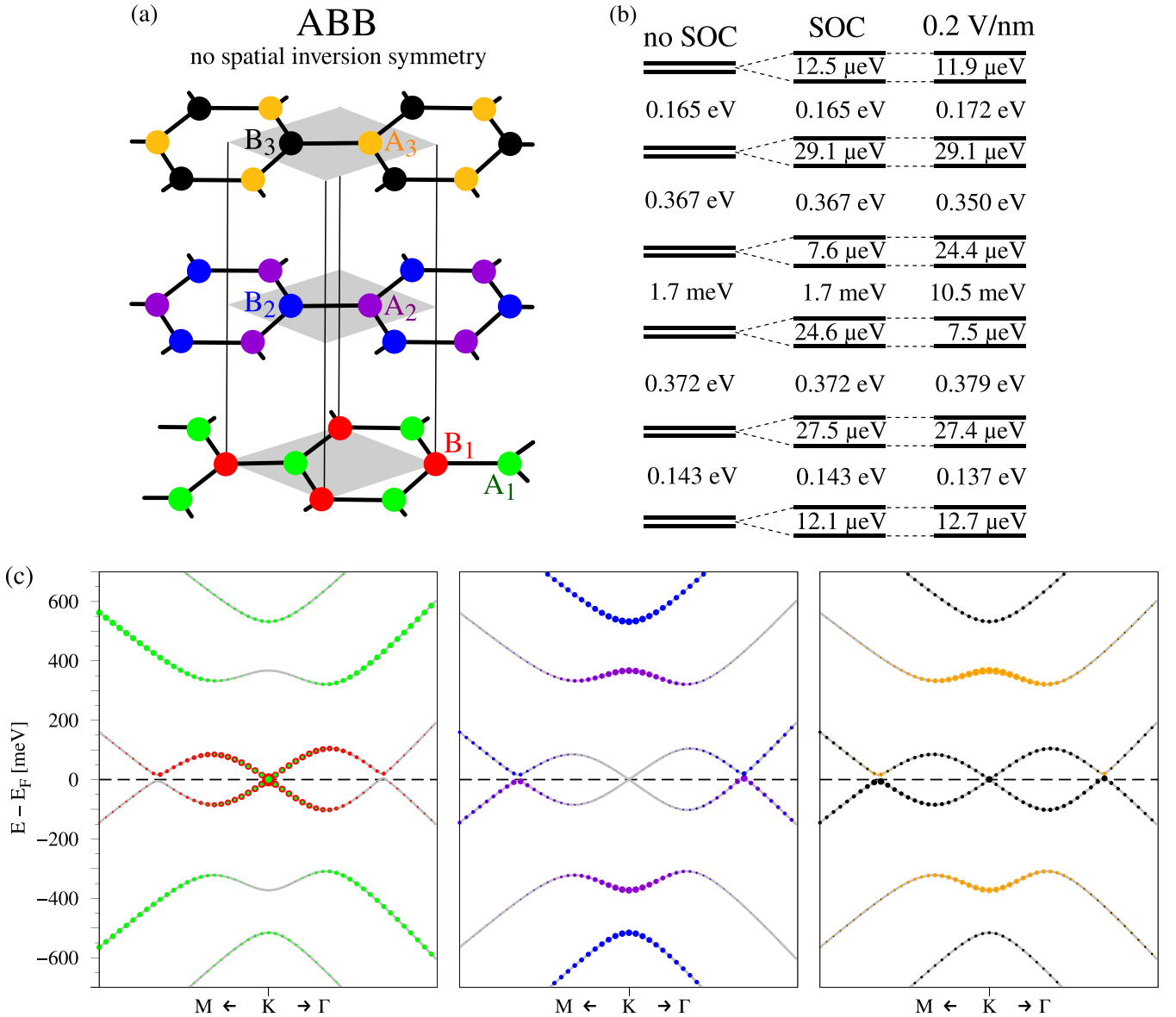


FIG. 3. (a) Lattice structure of the ABB TLG. Due to the absence of spatial inversion and  $z$ -mirror symmetry, all sublattice atoms are different (red, green, blue, purple, black, orange). Gray rhombuses define the unit cells of the layers. (b) The energy level diagram of states at the  $K$  point without SOC, with SOC, and with SOC in the presence of a transverse electric field of 0.2 V/nm. (c) The DFT-calculated band structure in the vicinity of the  $K$  point without SOC. From left to right, we project onto the different basis atoms from the three graphene layers, with the color code as defined in (a).

by  $3 \times 3$  monolayer supercells of bottom  $\text{MoSe}_2$  and top  $\text{WSe}_2$ . In the case of TMDC encapsulation, we use the lattice constant of pristine TLG (2.46 Å), and the  $\text{MoSe}_2$  and  $\text{WSe}_2$  lattice constants are barely strained (below 0.3% [114,115]) to 3.28 Å. Moreover, in the case of TMDC encapsulation, the twist angles between all layers are  $0^\circ$ . Here, we do not investigate different twist angles. Note that the electronic structures of TMDCs are very sensitive to strain [116], especially in terms of band gap. In contrast, the Dirac states of graphene are quite robust against biaxial strain [117,118]. Moreover, upon twisting, proximity SOC in graphene/TMDC heterostructures can be strongly modified, which has been investigated in Refs. [34,41,119]. Especially in Ref. [41], DFT calculations have shown that straining graphene, while leaving the TMDC unstrained, determines the position of the Dirac states within

the TMDC band gap. This band offset can be tuned by gating, thereby influencing proximity SOC. We believe that these findings would also apply for our heterostructures of TMDC encapsulated TLG.

In addition, we consider  $5 \times 5$  supercells of TLG to be encapsulated within  $\sqrt{3} \times \sqrt{3}$  supercells of ferromagnetic CGT. In the case of CGT encapsulation, we also keep the lattice constant of pristine TLG but stretch the CGT lattice constant by roughly 4% from 6.8275 Å [120] to 7.1014 Å for better comparability of the encapsulation cases. Note that, similar to the TMDCs, CGT also shows a strain-tunable band gap [121–123]. Again, the twist angle is crucial for proximity exchange in graphene/CGT heterostructures [40]. In our geometries, the relative twist angle between the top (bottom) CGT and the top (bottom) graphene layer is  $30^\circ$ . In Ref. [40],

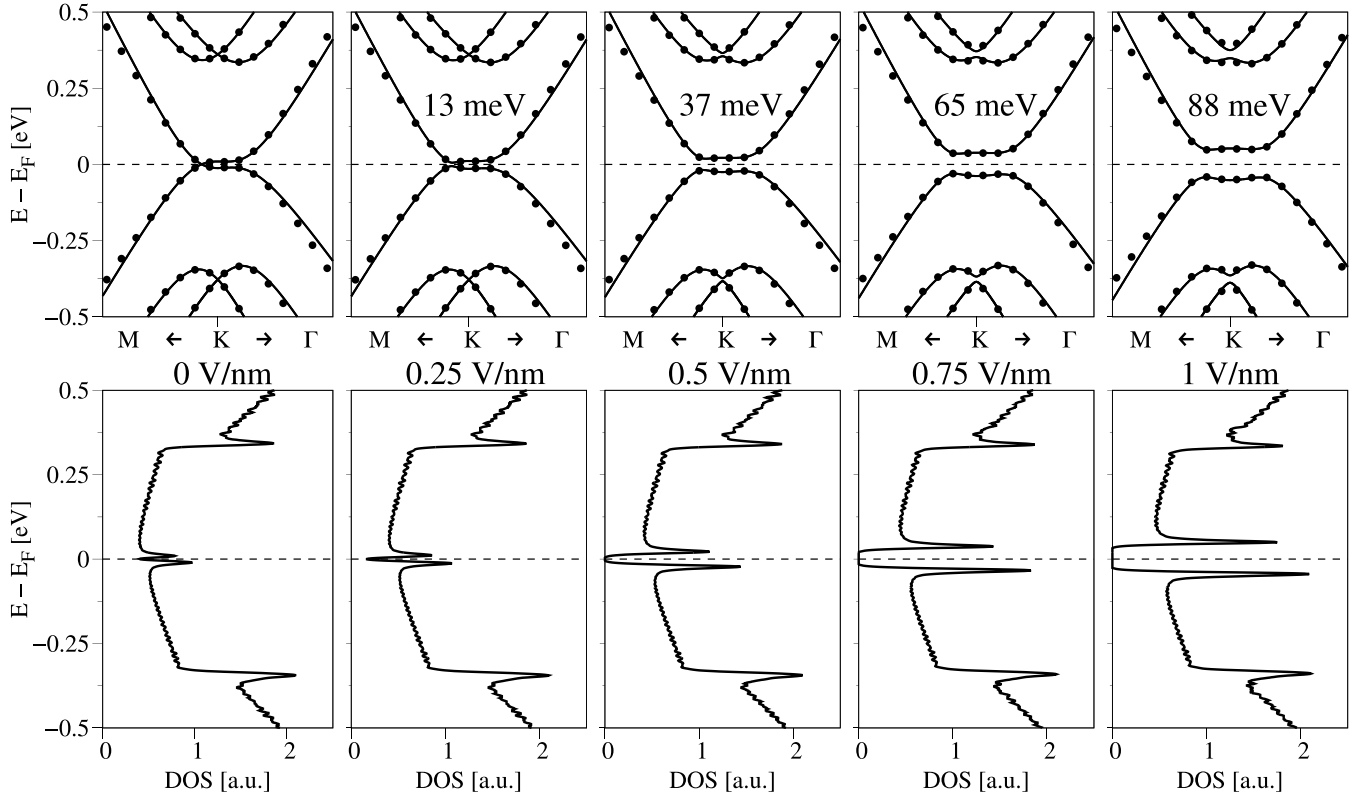


FIG. 4. Top: Zooms to the ABC TLG bands in the vicinity of the  $K$  point. We compare DFT data (symbols) with model Hamiltonian fits (solid lines) employing parameters from Table III in Appendix A. In the dispersion, we specify the band gap at the Fermi level. Bottom: The corresponding calculated density of states (DOS). From left to right, we increase the transverse electric field from 0 to 1 V/nm.

it has been explicitly shown by DFT calculations that mainly twisting influences proximity exchange, while straining determines the position of the graphene Dirac states within the CGT band gap. This band offset is again tunable by gating, thereby influencing proximity exchange. Also these findings should be applicable for our TLG structures.

Initial atomic structures are set up with the atomic simulation environment (ASE) [124] and visualized with VESTA

software [125]; see Fig. 5. Our choice of the encapsulating monolayers is based on the fact that TMDCs and CGT are semiconductors, providing strong spin-orbit and exchange couplings to graphene, correspondingly [12,24,25,54,60]. Another important factor for our choice is the lattice matching, such that the different materials can be combined in commensurate supercells for periodic DFT calculations, without straining them beyond reasonable limits.

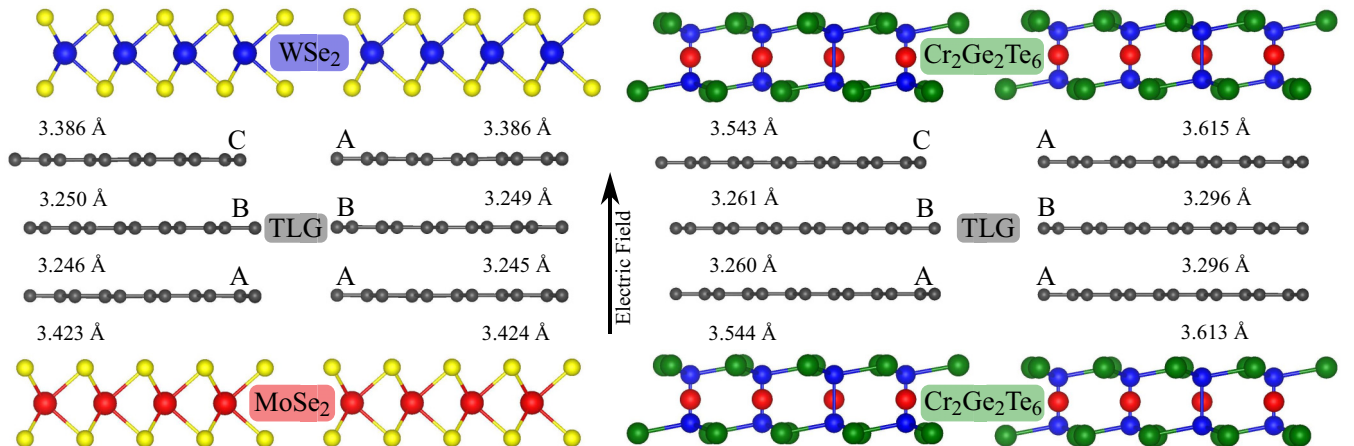


FIG. 5. Geometries of the encapsulated TLG heterostructures. Left: TMDC (MoSe<sub>2</sub> and WSe<sub>2</sub>) encapsulated ABA and ABC TLG. Right: CGT encapsulated ABA and ABC TLG. The relaxed interlayer distances are indicated. We also specify the direction of a positive electric field.

### B. Computational details

The electronic structure calculations and structural relaxations of the TLG-based vdW heterostructures are performed by DFT [126] with QUANTUM ESPRESSO [127]. Self-consistent calculations are performed with the  $k$ -point sampling of  $18 \times 18 \times 1$  to get converged results for the proximity-induced exchange and SOC. We use an energy cutoff for the charge density of 520 Ry, and the kinetic energy cutoff for wave functions is 65 Ry for the scalar relativistic pseudopotentials with the projector augmented wave method [128] with the Perdew-Burke-Ernzerhof exchange correlation functional [102]. In the case of CGT encapsulation, we perform open-shell calculations that provide the spin-polarized ground state and proximity exchange coupling. In addition, a Hubbard parameter of  $U = 1$  eV is used for Cr  $d$ -orbitals, similar to recent calculations [12,60,129]. In the case of TMDC encapsulation, we use the relativistic versions of the pseudopotentials to capture (proximity) SOC effects.

For the relaxation of the heterostructures, we add DFT-D2 vdW corrections [130,131] and use a quasinewton algorithm based on trust radius procedure. Dipole corrections [132] are also included to get correct band offsets and internal electric fields. To simulate quasi-2D systems, we add a vacuum of

20 Å to avoid interactions between periodic images in our slab geometries. To determine the interlayer distances, the atoms of TLG and the TMDCs are allowed to relax only in their  $z$  positions (vertical to the layers), and the atoms of CGT are allowed to move in all directions, until all components of all forces are reduced below  $10^{-3}$  (Ry/ $a_0$ ), where  $a_0$  is the Bohr radius. The obtained interlayer distances are summarized in Fig. 5 and are similar to previous reports [12,52,54]. Since we have assumed perfectly aligned individual layers, the full heterostructures still have  $C_3$  symmetry after relaxation.

### IV. MODEL HAMILTONIANS

Here we present the Hamiltonians that we employ to model the low-energy bands of the (encapsulated) ABA and ABC TLG. The basis states are  $|C_{A1}, s\rangle$ ,  $|C_{B1}, s\rangle$ ,  $|C_{A2}, s\rangle$ ,  $|C_{B2}, s\rangle$ ,  $|C_{A3}, s\rangle$ ,  $|C_{B3}, s\rangle$ , providing 12 eigenvalues  $\varepsilon_{1-12}$ , for both spin species  $s = \{\uparrow, \downarrow\}$  of each C atom. In this basis, the Hamiltonian comprises several terms [69,70,108,109,133],

$$\mathcal{H} = \mathcal{H}_{\text{orb}} + \mathcal{H}_{\text{soc}} + \mathcal{H}_{\text{ex}} + E_D. \quad (1)$$

The orbital terms for ABA and ABC TLG consist of  $p_z$  intra- and interlayer hoppings,

$$\mathcal{H}_{\text{orb}}^{\text{ABA}} = \begin{pmatrix} \Delta + V_1 & \gamma_0 f(\mathbf{k}) & \gamma_4 f^*(\mathbf{k}) & \gamma_1 & \gamma_5 & 0 \\ \gamma_0 f^*(\mathbf{k}) & \eta + V_1 & \gamma_3 f(\mathbf{k}) & \gamma_4 f^*(\mathbf{k}) & 0 & \gamma_2 \\ \gamma_4 f(\mathbf{k}) & \gamma_3 f^*(\mathbf{k}) & V_2 & \gamma_0 f(\mathbf{k}) & \gamma_4 f(\mathbf{k}) & \gamma_3 f^*(\mathbf{k}) \\ \gamma_1 & \gamma_4 f(\mathbf{k}) & \gamma_0 f^*(\mathbf{k}) & \Delta + V_2 & \gamma_1 & \gamma_4 f(\mathbf{k}) \\ \gamma_5 & 0 & \gamma_4 f^*(\mathbf{k}) & \gamma_1 & \Delta - V_1 & \gamma_0 f(\mathbf{k}) \\ 0 & \gamma_2 & \gamma_3 f(\mathbf{k}) & \gamma_4 f^*(\mathbf{k}) & \gamma_0 f^*(\mathbf{k}) & \eta - V_1 \end{pmatrix} \otimes s_0, \quad (2)$$

$$\mathcal{H}_{\text{orb}}^{\text{ABC}} = \begin{pmatrix} \Delta + V_1 & \gamma_0 f(\mathbf{k}) & \gamma_4 f^*(\mathbf{k}) & \gamma_1 & 0 & 0 \\ \gamma_0 f^*(\mathbf{k}) & \eta + 2V_1 & \gamma_3 f(\mathbf{k}) & \gamma_4 f^*(\mathbf{k}) & \gamma_6 & 0 \\ \gamma_4 f(\mathbf{k}) & \gamma_3 f^*(\mathbf{k}) & \Delta + V_2 & \gamma_0 f(\mathbf{k}) & \gamma_4 f^*(\mathbf{k}) & \gamma_1 \\ \gamma_1 & \gamma_4 f(\mathbf{k}) & \gamma_0 f^*(\mathbf{k}) & \Delta + 2V_2 & \gamma_3 f(\mathbf{k}) & \gamma_4 f^*(\mathbf{k}) \\ 0 & \gamma_6 & \gamma_4 f(\mathbf{k}) & \gamma_3 f^*(\mathbf{k}) & \eta - V_1 & \gamma_0 f(\mathbf{k}) \\ 0 & 0 & \gamma_1 & \gamma_4 f(\mathbf{k}) & \gamma_0 f^*(\mathbf{k}) & \Delta - V_1 \end{pmatrix} \otimes s_0. \quad (3)$$

The spin-orbit coupling and exchange terms are the same for both stackings in the above basis:

$$\mathcal{H}_{\text{soc}} + \mathcal{H}_{\text{ex}} = \begin{pmatrix} (\tau \lambda_I^{A1} - \lambda_{\text{ex}}^{A1}) s_z & 2i\lambda_{R1} s_-^\tau & 0 & 0 & 0 & 0 \\ -2i\lambda_{R1} s_+^\tau & (-\tau \lambda_I^{B1} - \lambda_{\text{ex}}^{B1}) s_z & 0 & 0 & 0 & 0 \\ 0 & 0 & 0 & 0 & 0 & 0 \\ 0 & 0 & 0 & 0 & 0 & 0 \\ 0 & 0 & 0 & 0 & (\tau \lambda_I^{A3} - \lambda_{\text{ex}}^{A3}) s_z & 2i\lambda_{R3} s_-^\tau \\ 0 & 0 & 0 & 0 & -2i\lambda_{R3} s_+^\tau & (-\tau \lambda_I^{B3} - \lambda_{\text{ex}}^{B3}) s_z \end{pmatrix}. \quad (4)$$

We use the linearized version of the nearest-neighbor structural function  $f(\mathbf{k}) = -(\sqrt{3}a/2)(\tau k_x - ik_y)$ , with the

graphene lattice constant  $a$  and the Cartesian wave vector components  $k_x$  and  $k_y$  measured from  $\pm K$  for the

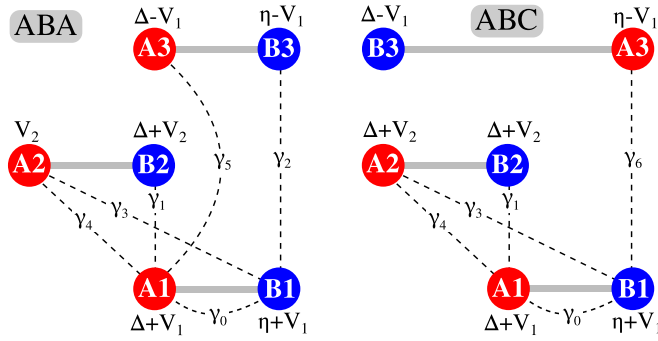


FIG. 6. Schematic illustration of the ABA (left) and ABC (right) TLG lattices, showing the relevant intra- and interlayer hoppings  $\gamma_j$ ,  $j = \{0, 1, 2, 3, 4, 5, 6\}$  (dashed lines). In addition, the bottom (top) graphene layer is placed in the potential  $V_1$  ( $-V_1$ ), while the middle layer is placed in potential  $V_2$ . The asymmetries  $\Delta$  and  $\eta$  arise due to vertical hoppings.

valley indices  $\tau = \pm 1$ . The Pauli spin matrices are  $s_i$ , with  $i = \{0, x, y, z\}$ , and  $s_{\pm}^{\tau} = (s_x \pm i\tau s_y)/2$ . Here,  $\gamma_j$ ,  $j = \{0, 1, 2, 3, 4, 5, 6\}$ , describe intra- and interlayer hoppings in TLG; see Fig. 6 for an overview. The coupling  $\gamma_0$  is the nearest-neighbor intralayer hopping amplitude between A and B sublattices within each graphene layer. The parameter  $\gamma_1$  describes the direct interlayer hopping between A and B sublattices of adjacent graphene layers. Similarly, parameters  $\gamma_2$ ,  $\gamma_5$ , and  $\gamma_6$  are also vertical interlayer hoppings, but between the outermost layers in TLG. In addition, the hoppings  $\gamma_3$  and  $\gamma_4$  are interlayer couplings, but not vertical. They connect next-nearest-neighbor atoms of adjacent graphene layers. Vertical hoppings in TLG couple only two atoms, hence they appear without structural function in the Hamiltonian, while the other hoppings couple an atom to three corresponding partner atoms, hence they appear linear in momentum.

In general, due to the proximity effect the three layers experience different energy potentials, which we describe by assigning  $V_2$  to the middle layer and  $\pm V_1$  to the outer layers. In addition, asymmetries  $\Delta$  and  $\eta$  arise due to the vertical hoppings ( $\gamma_1$  and  $\gamma_6$  in ABC TLG;  $\gamma_1$ ,  $\gamma_2$ , and  $\gamma_5$  in ABA TLG). The combination of parameters  $V_1$ ,  $V_2$ ,  $\Delta$ , and  $\eta$  can then describe the on-site energies of the individual sublattices of the different layers within TLG. The parameters  $\lambda_l$  ( $\lambda_{ex}$ ) describe the intrinsic or proximity-induced spin-orbit or exchange couplings of the corresponding layer and sublattice atom ( $C_{A1}$ ,  $C_{B1}$ ,  $C_{A3}$ ,  $C_{B3}$ ). The parameters  $\lambda_{Rl}$  represent the Rashba terms of the bottom and top layers  $l = \{1, 3\}$ . The middle layer, formed by atoms  $C_{A2}$  and  $C_{B2}$ , is far away from the proximitizing TMDC and CGT encapsulation layers. Therefore, we can neglect the corresponding proximity SOC and exchange parameters, as we will see from the band-structure fits. Actually, in the ABC TLG orbital Hamiltonian, the additional factors of 2 in front of  $V_1$  and  $V_2$  in the diagonal entries arise due to SOC [69] and are relevant for the spin-orbit gaps in the high-energy bands; see the energy level diagram in Fig. 2. To capture doping effects from the calculations, we introduce another parameter  $E_D$ , which leads to an energy shift of the model band structure.

Finally, to extract the fit parameters from the DFT, we employ a least-squares routine, taking into account band ener-

gies, splittings, and spin expectation values. In each case, we first fix the orbital parameters from fitting the dispersion, and then we fit band splittings and spin expectation values to find the spin-orbit and exchange parameters.

## V. BAND STRUCTURE AND FIT RESULTS

### A. TLG encapsulated within WSe<sub>2</sub> and MoSe<sub>2</sub>

Monolayer TMDCs are direct-band-gap semiconductors with strong SOC. Due to the proximity of graphene to a TMDC, a significant amount of SOC is introduced in graphene, leading to a splitting of the Dirac states on the order of 1 meV. In the case of TMDC-encapsulated TLG, only the outer graphene layers experience proximity coupling, due to the short-rangedness of the proximity effect in vdW heterostructures. This will lead to spin splittings in the TLG band structure, associated with bands originating from the top and bottom layer sublattice atoms.

#### 1. MoSe<sub>2</sub>/ABA-TLG/WSe<sub>2</sub> stacks

We start our discussion by considering the dispersion of the MoSe<sub>2</sub>/ABA-TLG/WSe<sub>2</sub> heterostructure; see Fig. 7(a). We find that the ABA TLG band structure, featuring the aforementioned 12 energy bands near the  $K$  point, is nicely preserved within this heterostructure. Here, we are mainly interested in the eight low-energy bands [see Fig. 7(b)], which resemble a combination of single- and bilayer-graphene low-energy spectra. Similar to BLG, the parabolic high-energy bands located at around  $\pm 0.5$  eV are mainly formed by states from dimer atoms  $A_1$ ,  $B_2$ , and  $A_3$  (see Fig. 21 in Appendix D) and are split off from the Fermi level due to the interlayer hopping  $\gamma_1$ . The low-energy bands are mainly formed by the nondimer atoms  $B_1$ ,  $A_2$ , and  $B_3$ , but one of them also contains contributions from  $A_1$  and  $A_3$  atoms.

The band structure and spin expectation values [see Figs. 7(b) and 7(c)] are nicely fitted by our model Hamiltonian employing the parameters in Table I. The proximity-induced SOC parameters are also as expected, giving valley-Zeeman and opposite Rashba couplings for top and bottom graphene layers. Because the bottom graphene layer couples to MoSe<sub>2</sub>, the values of the corresponding SOC parameters ( $\lambda_l$  and  $\lambda_R$ ) are smaller compared to the values for the top graphene layer, which couple to WSe<sub>2</sub>. This result is in agreement with findings from single-layer-graphene/TMDC heterostructures [25]. In addition, the middle layer experiences no proximity SOC, in agreement with BLG/TMDC results [54], where only adjacent layers are proximitized. The two Rashba SOC are opposite, because the bottom (top) graphene effectively feels the presence of a strong spin-orbit substrate (capping) layer, leading to opposite distortion of the corresponding  $p_z$  orbitals.

#### 2. MoSe<sub>2</sub>/ABC-TLG/WSe<sub>2</sub> stacks

Next, we analyze the dispersion of the MoSe<sub>2</sub>/ABC-TLG/WSe<sub>2</sub> heterostructure; see Fig. 8(a). Again, the bands near the  $K$  point closely resemble those from bare ABC-stacked TLG, but now with proximity SOC due to the surrounding TMDC layers. In contrast to ABA TLG, here we have eight high-energy bands at around  $\pm 0.4$  eV, which are again formed by the dimer atoms in the structure, i.e., by



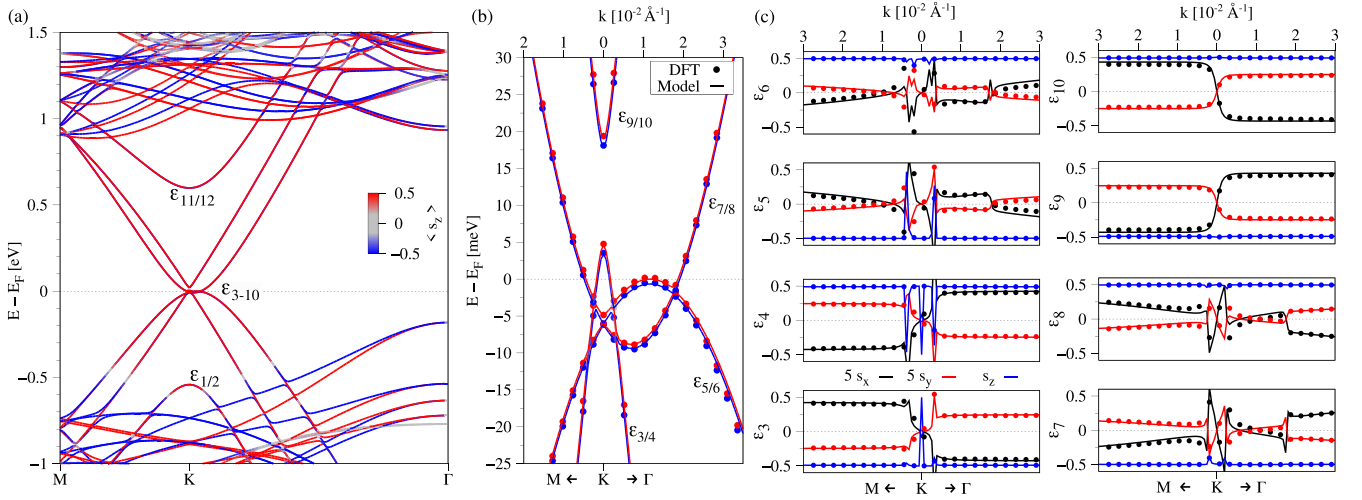


FIG. 7. (a) DFT-calculated band structure of the  $\text{MoSe}_2/\text{ABA-TLG}/\text{WSe}_2$  heterostructure along the  $M$ - $K$ - $\Gamma$  path. The color of the bands corresponds to the  $s_z$  spin expectation value. We specify the 12 relevant energy bands,  $\epsilon_{1-12}$ , corresponding to TLG, which seem to be pairwise spin-degenerate. (b) Zoom to the calculated low-energy bands (symbols) around the  $K$  point, corresponding to the band structure in (a), with a fit to the model Hamiltonian (solid lines). The bands are spin-split due to proximity-induced SOC. (c) The spin expectation values of the eight low-energy bands as labeled in (b). The  $s_x$  and  $s_y$  values are multiplied by a factor of 5 for better visualization.

the atoms  $A_1$ ,  $A_2$ ,  $B_2$ , and  $B_3$  (see Fig. 22 in Appendix D). The remaining four low-energy bands are formed by nondimer atoms  $B_1$  and  $A_3$ , which are coupled by the hopping  $\gamma_6$ . In

addition, they feature a conelike band touching along the  $K \rightarrow M$  direction. Again, the bands and spin expectation values can be nicely reproduced by our model [see Figs. 8(b) and 8(c)]

TABLE I. The fit parameters of the model Hamiltonian  $\mathcal{H}$  for the TMDC and the CGT encapsulated TLG structures. The arrows indicate the magnetization direction of CGT.

System	WSe <sub>2</sub> ABC MoSe <sub>2</sub>	WSe <sub>2</sub> ABA MoSe <sub>2</sub>	CGT $\uparrow$ ABC CGT $\uparrow$	CGT $\downarrow$ ABC CGT $\uparrow$	CGT $\uparrow$ ABA CGT $\uparrow$	CGT $\downarrow$ ABA CGT $\uparrow$
$\gamma_0$ (eV)	2.5307	2.5482	2.5048	2.5200	2.5412	2.5375
$\gamma_1$ (eV)	0.4014	0.4028	0.3899	0.3898	0.3612	0.3585
$\gamma_2$ (eV)	0	-0.0119	0	0	-0.0099	-0.0101
$\gamma_3$ (eV)	0.3292	0.3102	-0.3287	-0.3341	-0.2926	-0.2926
$\gamma_4$ (eV)	-0.1838	-0.1765	-0.1755	-0.1778	-0.1723	-0.1727
$\gamma_5$ (eV)	0	0.0181	0	0	0.0076	0.0049
$\gamma_6$ (eV)	0.0125	0	-0.0113	-0.0116	0	0
$V_1$ (meV)	0.027	0.077	0.116	-0.170	-0.530	-0.076
$V_2$ (meV)	-11.022	-6.278	-12.045	-7.469	-3.264	-2.952
$\Delta$ (meV)	7.961	22.084	11.095	6.937	10.162	7.583
$\eta$ (meV)	-3.121	6.572	-2.831	-3.076	4.494	4.484
$\lambda_{R1}$ (meV)	0.233	0.215	0	0	0	0
$\lambda_{R3}$ (meV)	-0.475	-0.459	0	0	0	0
$\lambda_I^{A1}$ (meV)	0.209	0.204	0	0	0	0
$\lambda_I^{B1}$ (meV)	-0.204	-0.206	0	0	0	0
$\lambda_I^{A3}$ (meV)	1.125	0.995	0	0	0	0
$\lambda_I^{B3}$ (meV)	-0.983	-1.011	0	0	0	0
$\lambda_{ex}^{A1}$ (meV)	0	0	-3.393	-3.393	-3.210	-3.210
$\lambda_{ex}^{B1}$ (meV)	0	0	-3.393	-3.393	-3.210	-3.210
$\lambda_{ex}^{A3}$ (meV)	0	0	-3.349	3.349	-3.210	3.210
$\lambda_{ex}^{B3}$ (meV)	0	0	-3.349	3.349	-3.210	3.210
$E_D$ (meV)	-4.171	0	5.540	10.605	0	0
dipole (Debye)	-0.0152	-0.0109	-0.0110	0.0010	0.0087	0.0101

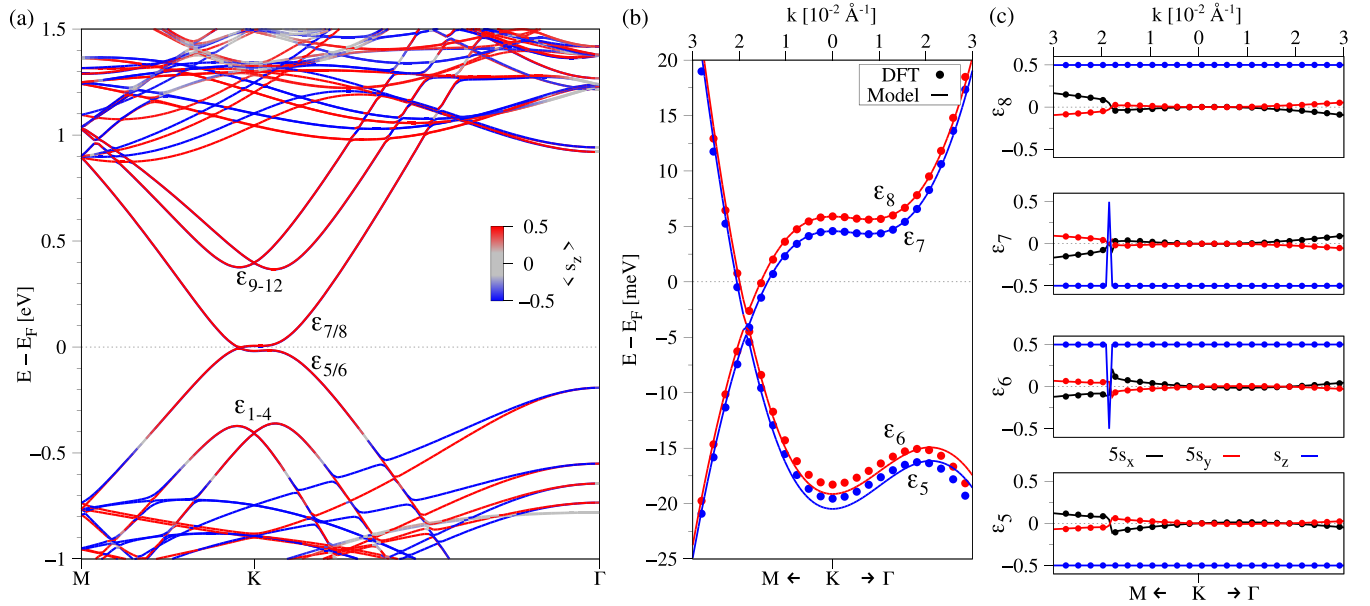


FIG. 8. (a) DFT-calculated band structure of the  $\text{MoSe}_2/\text{ABC-TLG}/\text{WSe}_2$  heterostructure along the  $M$ - $K$ - $\Gamma$  path. The color of the bands corresponds to the  $s_z$  spin expectation value. We specify the 12 relevant energy bands,  $\epsilon_{1-12}$ , corresponding to TLG, which seem to be pairwise spin-degenerate. (b) Zoom to the calculated low-energy bands (symbols) around the  $K$  point, corresponding to the band structure in (a), with a fit to the model Hamiltonian (solid lines). The bands are spin-split due to proximity-induced SOC. (c) The spin expectation values of the four low-energy bands as labeled in (b). The  $s_x$  and  $s_y$  values are multiplied by a factor of 5 for better visualization.

employing the fit parameters from Table I. Similar to BLG, the low-energy bands of ABC TLG can be strongly tuned by an electric field (in terms of band gap; see Fig. 4) [69], since only two sublattice atoms from different layers contribute. The electric field tunability of the heterostructure dispersion will be investigated later. Similar to the ABA heterostructure, proximity-induced SOC are of valley-Zeeman type and the outermost layers experience opposite Rashba couplings. The spin-orbit fields (see Fig. 9), corresponding to the low-energy bands  $\epsilon_{5-8}$ , are mainly  $s_z$ -polarized, but they show a Rashba texture especially around the conelike touching points along the  $K \rightarrow M$  direction. The band touching should actually determine the Fermi level. However in Fig. 8, we have a small amount of doping ( $E_D \neq 0$ ), due to the finite  $k$ -point sampling of the Brillouin zone in the DFT calculation. We therefore fix  $E_D$  from the DFT before we apply our fitting procedure.

### B. TLG encapsulated within magnetic $\text{Cr}_2\text{Ge}_2\text{Te}_6$

We now turn to proximity exchange, and we consider TLG in ABA and ABC stacking encapsulated by the ferromagnetic semiconductor CGT. Again, the outermost graphene layers will experience proximity couplings, now stemming from the exchange interaction. In general, top and bottom graphene layers can feel different exchange fields. We investigate both parallel and antiparallel magnetizations of the encapsulating CGT layers, and we analyze the consequences for the TLG low-energy bands.

#### 1. CGT/ABA/CGT stacks

We first address the ABA TLG, sandwiched between two CGT layers. In Fig. 10(a) we show the calculated global band structure of the CGT/ABA-TLG/CGT heterostructure

for parallel CGT magnetizations. In particular, the ABA TLG low-energy bands can be nicely recognized near the Fermi level. The high-energy conduction bands of TLG are located within the CGT conduction bands. In addition, we find

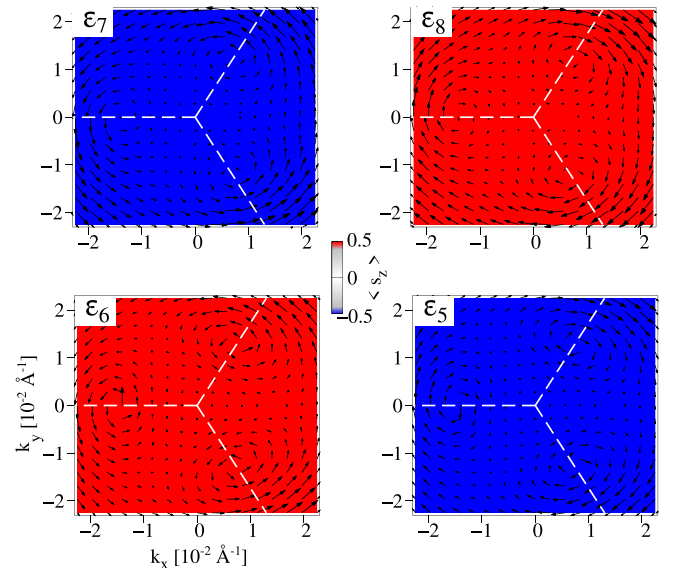


FIG. 9. First-principles calculated spin-orbit fields around the  $K$  point of the  $\text{MoSe}_2/\text{ABC-TLG}/\text{WSe}_2$  heterostructure, corresponding to the four low-energy bands  $\epsilon_5$ – $\epsilon_8$  in Fig. 12 at zero electric field. The dashed white lines represent the edges of the hexagonal Brillouin zone with the  $K$  point at the center ( $k_x = k_y = 0$ ). The  $s_z$  spin expectation value determines the color, while in-plane spins are depicted as arrows. Here, we enhanced in-plane spin expectation values by a factor of 10 for better visualization.

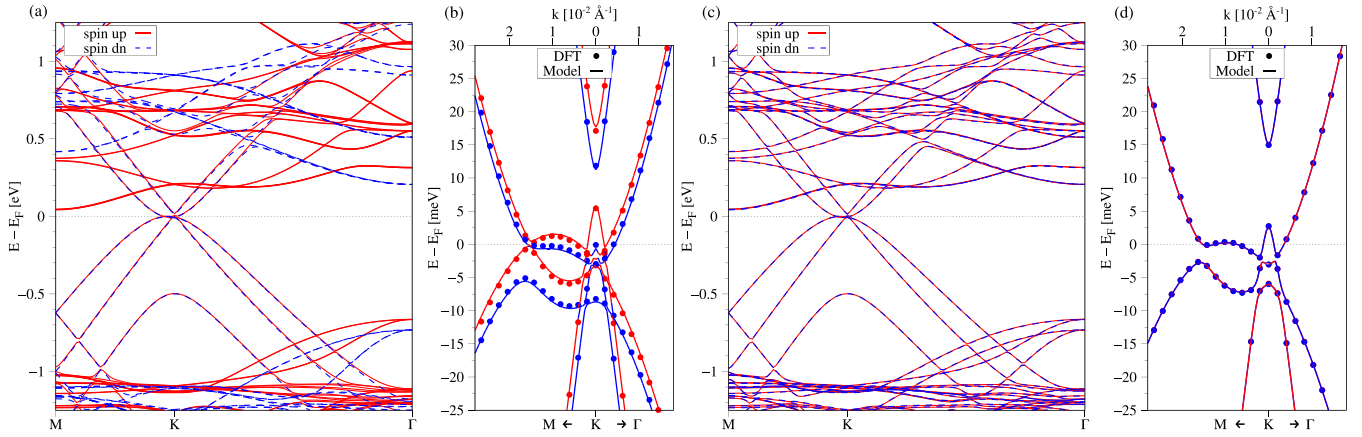


FIG. 10. (a) Band structure of the CGT/ABA-TLG/CGT heterostructure along the  $M$ - $K$ - $\Gamma$  path. Bands in solid red (dashed blue) correspond to spin up (spin down). The two CGT layers have parallel magnetizations along the  $z$  direction. (b) Zoom to the calculated low-energy bands (symbols) around the  $K$  point, corresponding to the band structure in (a), with a fit to the model Hamiltonian (solid lines). (c),(d) Same as (a),(b) but for antiparallel magnetization of the two CGT layers (bottom layer along  $z$ , top layer along  $-z$ ).

spin-polarized bands close to the Fermi level near the  $M$  point, originating from the CGT layers. Zooming in on the Fermi level near the  $K$  point, we again recognize the eight low-energy bands originating from ABA TLG; see Fig. 10(b). Similar to the TMDC encapsulation, the bands are also significantly split, but now due to the exchange coupling originating from the ferromagnetic CGT layers. The bands can be nicely reproduced by our model Hamiltonian employing the fit parameters listed in Table I. In general, orbital parameters are barely affected by the surrounding materials proximitizing TLG, as can be seen by comparing with the fit results from the TMDC encapsulation. However, proximity-induced exchange couplings,  $\lambda_{\text{ex}}$ , are now necessary to capture the essential band-structure features. From the fit, we find uniform exchange parameters of about  $-3.4$  meV for all C sublattice atoms of the two outer graphene layers. This is in agreement with previous considerations for encapsulated BLG [54,60].

What happens if we switch the magnetization direction of one CGT layer? In Fig. 10(c), we show the calculated global band structure of the CGT/ABA-TLG/CGT heterostructure for antiparallel CGT magnetizations. In general, the band structure remains the same, but bands originating from the topmost CGT layer have switched their spin-polarization. Most important are the consequences for the TLG low-energy bands; see Fig. 10(d). For parallel magnetizations, the bands were spin-split due to uniform proximity-induced exchange couplings. By switching the magnetization direction of the top CGT layer, the proximity exchange of the topmost graphene layer also adapts and switches sign, as reflected in the fitted parameters; see Table I. Since the low-energy bands of TLG are equally formed by carbon atoms from top and bottom graphene layers, now with opposite proximity exchange couplings which effectively cancel each other, the bands remain spin-degenerate. Again, this is similar to that in CGT encapsulated BLG [60].

## 2. CGT/ABC/CGT stacks

Now, we turn to the CGT encapsulated ABC heterostructure. The band structure and fit results are summarized in

Fig. 11, again considering parallel or antiparallel magnetizations of the CGT layers. The low-energy bands of ABC TLG are located near the Fermi level, similar to the TMDC encapsulation. The touching point of the bands is now along the  $K \rightarrow \Gamma$  direction; see Fig. 11(b). In contrast, for the TMDC-encapsulated case, the touching was along the  $K \rightarrow M$  direction; see Fig. 8(b). This is related to the different supercell sizes of ABC TLG in the different encapsulation scenarios, and the backfolding of the graphene  $k$  points into the heterostructure Brillouin zone [134]. A similar observation can be made considering the ABA TLG band structures for the different encapsulations. Actually, the touching point should determine the Fermi level, but due to the finite  $k$ -point sampling in our DFT calculation, a small doping of about 5 meV appears.

Most important is the low-energy band structure, featuring four Dirac-like bands; see Fig. 11(b). In the parallel magnetization case, the bands are split due to uniform proximity-induced exchange coupling in the outermost graphene layers of ABC TLG. The model parameters from Table I perfectly reproduce the dispersion in the vicinity of the  $K$  point, featuring exchange parameters of about  $-3.2$  meV. Looking at the fitted orbital parameters, we find that  $\gamma_3$  and  $\gamma_6$  have the opposite sign but are nearly equal in value compared to the TMDC-encapsulated ABC structure. This is again related to the different supercells and the backfolding, as already explained.

What happens when we switch the magnetization direction of one CGT layer? In the antiparallel case [see Figs. 11(c) and 11(d)], the overall band structure is similar to the parallel magnetization. Again, bands originating from the topmost CGT layer have switched their spin-polarization. Most important are the consequences for the ABC TLG low-energy bands. They remain nearly spin-degenerate, since the proximity exchange couplings from the top and bottom graphene layer are again opposite in sign but nearly equal in value. In addition, a sizable gap opens at the former touching point, which originates from the layered antiferromagnetic proximity exchange in the outermost graphene layers of ABC TLG. This is similar to the observations we made in CGT encapsulated BLG [60].

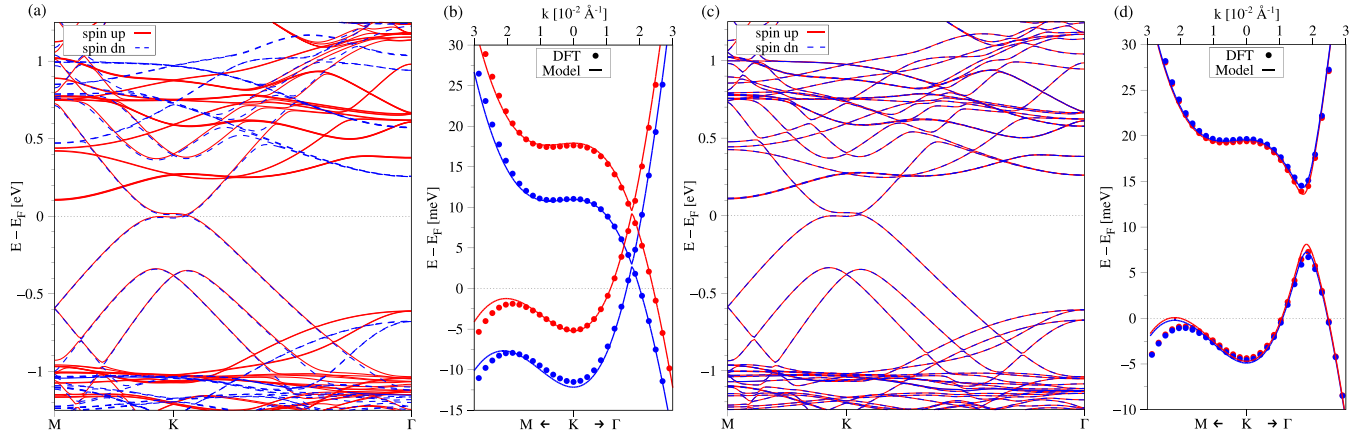


FIG. 11. (a) Band structure of the CGT/ABC-TLG/CGT heterostructure along the  $M$ - $K$ - $\Gamma$  path. Bands in solid red (dashed blue) correspond to spin up (spin down). The two CGT layers have parallel magnetizations along the  $z$  direction. (b) Zoom to the calculated low-energy bands (symbols) around the  $K$  point, corresponding to the band structure in (a), with a fit to the model Hamiltonian (solid lines). (c),(d) Same as (a),(b) but for antiparallel magnetization of the two CGT layers (bottom layer along  $z$ , top layer along  $-z$ ).

insulated BLG [60], where cancellation of proximity exchange or proximity SOC leads to a gap opening without an external electric field. Therefore, also in the TMDC encapsulated scenario, we could open the gap if proximity SOC from top and bottom graphene layers are opposite. This happens, for example, when employing the same TMDC layers for the encapsulation of ABC TLG, but with a relative twist angle of  $60^\circ$  between them.

Given the similarity of the low energy physics of BLG and ABC TLG, the recently proposed spin valve device concepts [58,135,136], which employ proximitized BLG, should also be applicable to ABC TLG. Most importantly, since the low-energy band splittings depend on the magnetic configuration of the outer magnetic layers, as well as on the applied transverse electric field, one can efficiently control the in-plane conductance in doubly proximitized ABC-TLG.

## VI. ELECTRIC FIELD TUNABILITY

Finally, we consider the electric field tunability of the low-energy bands of encapsulated TLG. The main effect of the field is that we place the outermost graphene layers in different potentials, thereby opening band gaps in the spectrum; see, for example, Fig. 4 for bare ABC TLG. In the following, we restrict ourselves to the case of TMDC encapsulation, since for the CGT case one can expect similar outcomes. More precisely, as we have seen above, the most striking difference between the CGT and TMDC encapsulation cases is that proximity exchange coupling, rather than proximity SOC, is responsible for the band splittings. From the model Hamiltonian perspective, see Table I, orbital parameters are barely different for the two encapsulation scenarios, while proximity exchange couplings,  $\lambda_{\text{ex}}$ , are about three times larger in magnitude compared to proximity SOC,  $\lambda_{\text{I}}$ . Therefore, one can expect a similar electric field behavior of the TLG low-energy bands in both encapsulations. In addition, below we restrict ourselves to consider small field values of  $\pm 0.25$  V/nm to capture the main effects of the field on the disper-

sion. In Fig. 5, we specify the direction of a positive electric field.

### A. MoSe<sub>2</sub>/ABC-TLG/WSe<sub>2</sub> stacks

In Fig. 12 we show the electric field evolution of the MoSe<sub>2</sub>/ABC-TLG/WSe<sub>2</sub> low-energy bands, including model fits. Since our model Hamiltonian very accurately reproduces the low-energy dispersions, we also show the corresponding DOS, calculated from the model [137]. When an electric field is applied across ABC TLG, a band gap opens at the conelike band touching along the  $K \rightarrow M$  line. The field separates the outer graphene layers in energy by the potential  $V_1$ . To fit the low-energy bands, when an electric field is applied, we keep the parameters from Table I fixed, but we refit the parameters  $\eta$  and  $V_1$ . The reason is that the applied field is small ( $\pm 0.25$  V/nm) and especially these two orbital parameters are relevant for the atoms  $B_1$  and  $A_3$ , forming the low-energy bands. With this approach, the band structures with electric field are almost perfectly reproduced by the model.

In addition, we note that for negative field, the conduction band is split much less than the valence band and vice versa for the positive field. This can also be seen by looking at the calculated DOS. Such a switching of band splittings reminds us of the BLG physics [52,54,57,60]. As theoretically proposed [52] and experimentally demonstrated [57], a transverse electric field, applied across a BLG/TMDC heterostructure, can efficiently tune SOC of conduction electrons, making it a potential platform for a spin-transistor. For ABC TLG, the low-energy bands are formed by atoms  $B_1$  and  $A_3$ , which experience different magnitudes of proximity SOC, as the corresponding spin-orbit parameters in Table I show. For positive electric field, the bottom graphene layer, which couples to MoSe<sub>2</sub>, sits in a lower potential than the top graphene layer, which couples to WSe<sub>2</sub>. Therefore, the valence band is mainly formed by atoms  $B_1$ , experiencing proximity SOC of about 0.2 meV, while the conduction band is formed by atoms  $A_3$ , having proximity SOC of about 1 meV. For negative electric field, the situation is reversed, allowing us to fully electrically



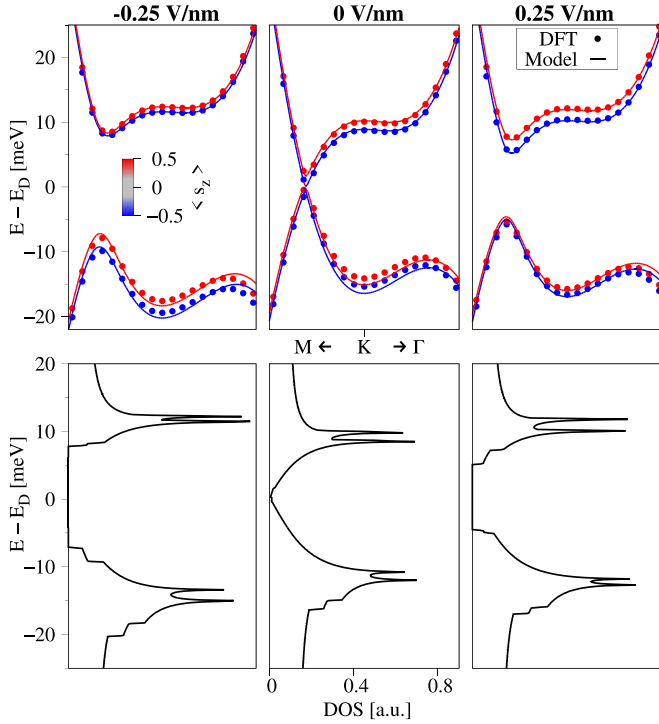


FIG. 12. Top: Electric field evolution of the low-energy bands of the  $\text{MoSe}_2/\text{ABC-TLG}/\text{WSe}_2$  heterostructure near the  $K$  point. The color of the bands corresponds to the  $s_z$  spin expectation value. From left to right, we tune the electric field from  $-0.25$  to  $0.25$  V/nm. The calculated low-energy bands (symbols) match well with the model Hamiltonian fits (solid lines). Bands are plotted with respect to the Dirac point energy  $E_D$ . For the  $\pm 0.25$  V/nm cases, we fixed the parameters from Table I and refitted the potential  $V_1$  and asymmetry  $\eta$ , since mainly these parameters are affected by a small electric field (see Table III). We obtained  $V_1 = 6.259$  ( $-3.839$ ) meV and  $\eta = -6.782$  ( $-0.771$ ) meV for the negative (positive) field. Bottom: The corresponding electric field evolution of the DOS, as calculated from the model Hamiltonian.

swap between the two magnitudes of SOC in the low-energy bands of ABC TLG. Such a swapping between spin-orbit splittings allows us to electrically control spin relaxation in proximitized ABC TLG.

### B. $\text{MoSe}_2/\text{ABA-TLG}/\text{WSe}_2$ stacks

The impact of a transverse electric field on the ABA bands and DOS is more complicated than for the ABC case; see Fig. 13. Here, we have eight low-energy bands that are present near the Fermi level, and which are formed by almost all carbon atoms from the three layers. Nevertheless, similar to ABC TLG, the electric field introduces a potential difference between the outermost graphene layers. In the model Hamiltonian, we capture this with parameter  $V_1$ . In addition, the middle layer can in general also sit in some nonzero potential, which we capture by  $V_2$ . Therefore, in order to fit the bands when an electric field is applied, we fix the parameters from Table I, but we refit the parameters  $V_1$  and  $V_2$ . Again, the band structures with electric field are also nicely reproduced by the model Hamiltonian, allowing us to calculate the DOS [137].

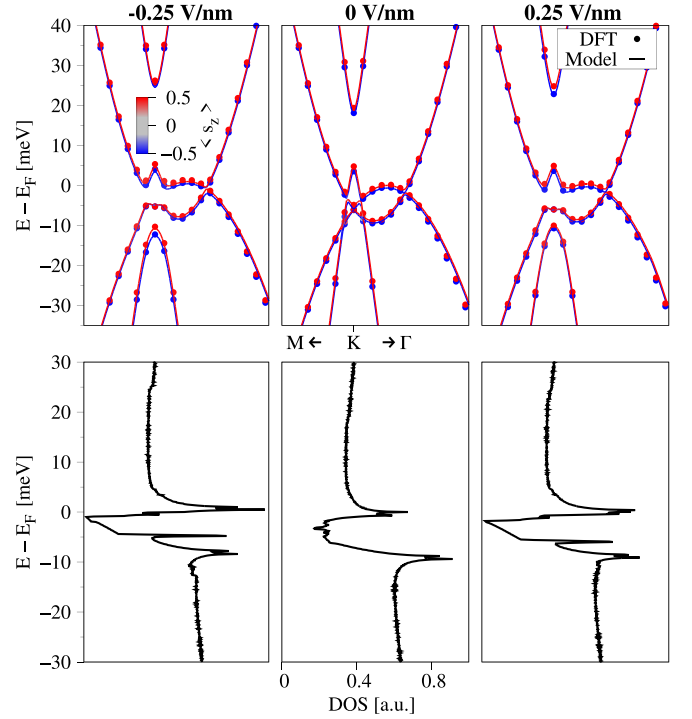


FIG. 13. Top: Electric field evolution of the low-energy bands of the  $\text{MoSe}_2/\text{ABA-TLG}/\text{WSe}_2$  heterostructure near the  $K$  point. The color of the bands corresponds to the  $s_z$  spin expectation value. From left to right, we tune the electric field from  $-0.25$  to  $0.25$  V/nm. The calculated low-energy bands (symbols) match well with the model Hamiltonian fits (solid lines). For the  $\pm 0.25$  V/nm cases, we fixed the parameters from Table I, and refitted the potentials  $V_1$  and  $V_2$ , since mainly these parameters are affected by a small electric field (see Table II). We obtained  $V_1 = 13.748$  ( $-12.021$ ) meV and  $V_2 = -4.984$  ( $-6.195$ ) meV for the negative (positive) field. Bottom: The corresponding electric field evolution of the DOS, as calculated from the model Hamiltonian.

With the small field amplitudes that we employ, the low-energy dispersion barely changes. Nevertheless, the Dirac-like bands are further separated in energy and now strongly anticross with the BLG-like bands. The parabolic bands still touch along the  $K \rightarrow \Gamma$  direction and the spectrum is not yet gapped for fields of  $\pm 0.25$  V/nm, as can be seen from the DOS.

## VII. INTERPLAY OF SPIN INTERACTIONS

One important conclusion of the previous discussion is that one can very well reproduce DFT data with our model Hamiltonians. The inclusion of an electric field, transverse to the monolayers, is straightforward, as it can be parametrized by essentially two orbital parameters. Considering also that the proximity effects are short-ranged, we can realistically study more complex structures, such as ex-so-tic CGT/TLG/TMDC heterostructures [92].

To be specific, we investigate TLG encapsulated by strong spin-orbit semiconductor  $\text{WSe}_2$  on the top, and ferromagnetic semiconductor CGT on the bottom. To calculate the dispersion from the model Hamiltonian, we use the orbital parameters from Table I of TMDC-encapsulated ABA and ABC TLG. In addition, we employ valley Zeeman and Rashba

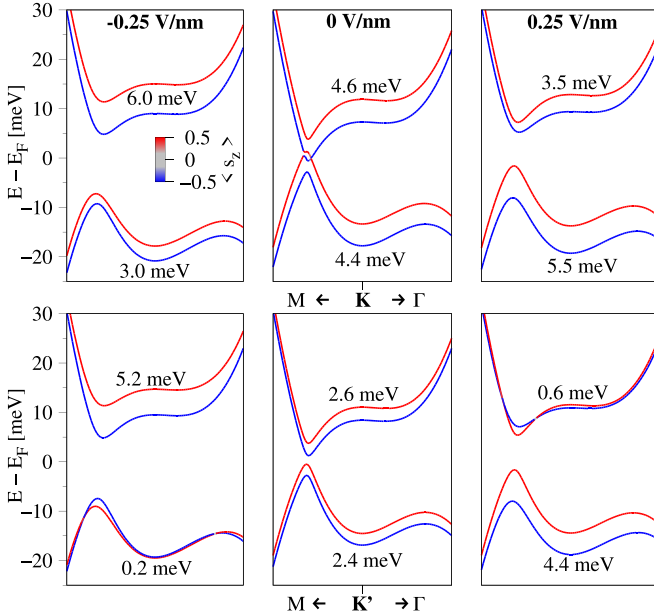


FIG. 14. Electric field evolution of the low-energy bands of a CGT/ABC-TLG/WSe<sub>2</sub> heterostructure near the  $K$  (top row) and  $K'$  (bottom row) points. The color of the bands corresponds to the  $s_z$  spin expectation value. From left to right, we tune the electric field from  $-0.25$  to  $0.25$  V/nm. Next to the bands, we list the spin splitting at the  $K/K'$  point. The dispersions are calculated from the model, assuming reasonable parameters as explained in the text.

SOC for the top graphene layer ( $\lambda_1^{A3} = -\lambda_1^{B3} = 1$  meV,  $\lambda_{R3} = -0.4$  meV), as well as exchange coupling for the bottom graphene layer ( $\lambda_{ex}^{A1} = \lambda_{ex}^{B1} = -3.5$  meV). This is a reasonable choice, according to our findings. To study the electric field behavior, also on the model level, we additionally employ the fitted parameters for the different electric fields ( $V_1$  and  $V_2$  for ABA;  $V_1$  and  $\eta$  for ABC); see Figs. 12 and 13. The combination of SOC and proximity exchange breaks time-reversal symmetry. Therefore, we calculated the dispersion near both the  $K$  and  $K'$  valleys.

#### A. ABC

The model results for ABC TLG are summarized in Fig. 14. For zero field, both sublattice atoms  $B_1$  and  $A_3$  are equally contributing to all four low-energy bands. The band splittings result now from the interplay of proximity spin-orbit and exchange couplings, originating from the individual layers. Consequently, at  $K$  ( $K'$ ), the two spin interactions are additive (subtractive) and band splittings are about 4.5 meV (2.5 meV). Moreover, we find that the ABC low-energy bands exhibit no gap near the  $K$  valley, while there is a gap near the  $K'$  valley (see Fig. 14), which is potentially important for the realization of a valley-polarized quantum anomalous Hall effect [17].

When an electric field is introduced, the bands are separated in energy, since the outermost layers are now in different potentials. In addition, the bands are no longer equally formed by the two sublattice atoms. Still, the different spin interactions are at interplay, either in an additive or subtractive way. Consequently, for positive field both bands are spin

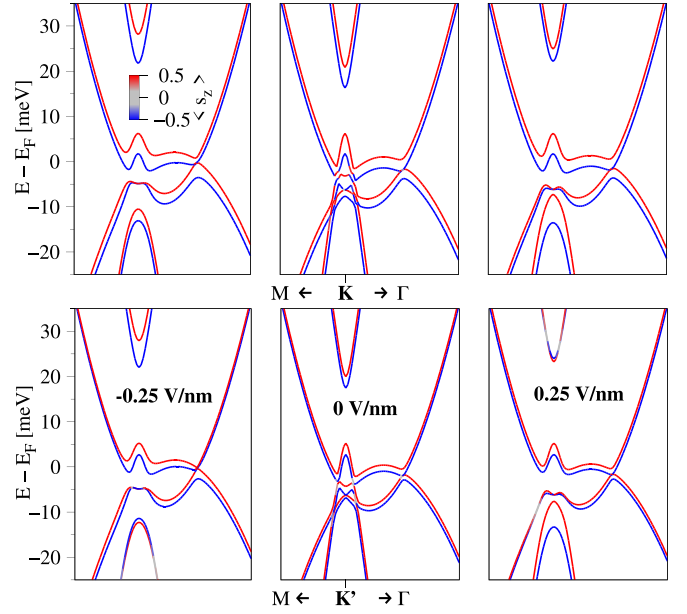


FIG. 15. Electric field evolution of the low-energy bands of a CGT/ABA-TLG/WSe<sub>2</sub> heterostructure near the  $K$  (top row) and  $K'$  (bottom row) points. The color of the bands corresponds to the  $s_z$  spin expectation value. From left to right, we tune the electric field from  $-0.25$  to  $0.25$  V/nm. The bands are calculated from the model, assuming reasonable parameters as explained in the text.

split at  $K$ , while at  $K'$  the valence band is strongly split and the conduction band stays nearly degenerate. Reversing the direction of the electric field, the bands are flipped with respect to the Fermi level, since also the potential difference is now opposite compared to the positive field. The fact that different magnitudes of splittings arise in different bands and valleys is important for the gate control of spin relaxation [52], potentially resulting in valley- and spin-polarized currents [17].

#### B. ABA

In Fig. 15, we show the calculated model low-energy dispersion of the ABA TLG when the two spin interactions are at interplay. For zero field, we observe a similar behavior as for the ABC TLG, where near  $K$  the band splittings are larger than near  $K'$ , due to additive/subtractive effects of the spin interactions. In addition, looking at the field evolution ( $-0.25 \rightarrow 0.25$  V/nm) of the Dirac-like bands, we observe a swapping of the nearly spin-degenerate bands from the valence into the conduction side at the  $K'$  valley, and vice versa for the strongly split bands. Similar observations can be made at the  $K$  valley. The BLG-like parabolic bands remain more or less the same with the applied field.

### VIII. SUMMARY

We have investigated systematically the electronic band structure of TLG in different stacking and encapsulation configurations. Starting with bare ABA, ABC, and ABB TLG, we have provided the essential ingredients of the orbital and spin-orbital effects, and both a quantitative and a qualitative

understanding of the SOC at the sub-meV level. Important for ongoing investigations, we also report on the electric-field tunability of the electronic DOS and VHS.

The bulk of our investigation is devoted to encapsulated TLG. We deal separately with proximity SOC and proximity exchange. The proximity SOC is studied by encapsulating ABA and ABC TLG within WSe<sub>2</sub> and MoSe<sub>2</sub>. We show how the two semiconducting monolayers affect the low-energy bands of TLG, inducing relatively strong (meV) spin splittings that are tunable by electric field. We also show that the effective model Hamiltonian, which considers sizable SOC on the outer layers, performs great in explaining the DFT results.

Proximity exchange is analyzed for the stacks of TLG encapsulated within CGT monolayers. The proximity exchange, also on a meV scale, modifies the low-energy bands of TLG, differently for parallel and antiparallel CGT magnetizations. The magnetic tunability should be a useful way to control correlated phases, especially in ABC TLG which exhibits a large DOS at low energies.

The nice comparison between the DFT results and the model makes us confident in applying the model itself in more complex situations, such as studying ex-so-tic CGT/TLG/TMDC heterostructures [92]. The interplay of spin-orbit and exchange coupling leads to a different band structure at  $K$  and  $K'$ . In addition, the layer polarization then allows for a strong tunability of the bands with a transverse electric field, which is able to close or open spin splittings, or even switch the spin polarization, for a particular band in encapsulated ABC TLG.

In all our investigated DFT cases, we provide fitting parameters to the effective model as a useful resource for subsequent investigations of transport and correlated physics based on realistic model simulations.

## ACKNOWLEDGMENTS

This work was funded by the Deutsche Forschungsgemeinschaft (DFG, German Research Foundation) SFB 1277 (Project No. 314695032), SPP 2244 (Project No. 443416183), and the European Union Horizon 2020 Research and Innovation Program under Contract No. 881603 (Graphene Flagship). M.G. acknowledges financial support provided by Slovak Research and Development Agency under Contract

No. APVV-20-0150 and by the Ministry of Education, Science, Research and Sport of the Slovak Republic provided under Grant No. VEGA 1/0105/20.

## APPENDIX A: ELECTRIC FIELD EFFECTS OF BARE ABA AND ABC TRILAYER GRAPHENE

The following electric field results for bare ABA and ABC TLG have been obtained with QUANTUM ESPRESSO [127]. We used the same structural input as for WIEN2K [96], as described in the main text. Self-consistent calculations are performed with the  $k$ -point sampling of  $240 \times 240 \times 1$  to accurately determine the Fermi level and the DOS. We used an energy cutoff for the charge density of 450 Ry, and the kinetic energy cutoff for wave functions is 55 Ry for the scalar relativistic pseudopotentials with the projector augmented wave method [128] with the Perdew-Burke-Ernzerhof exchange correlation functional [102]. Moreover, we added vdW [130,131] and dipole corrections [132].

Since we are mainly interested in the electric field behavior of the dispersion and the DOS, we neglect SOC since the induced splittings are on the  $\mu\text{eV}$  level (see the main text). In any case, the plane wave and pseudopotential method, implemented in QUANTUM ESPRESSO [127], cannot give correct spin-orbit splittings in graphene, since the relevant  $d$ -orbitals are missing [97,98]. Nevertheless, on an orbital level, the dispersions are the same as calculated with WIEN2K [96], and we can safely study the electric field tunability.

The fit parameters from Tables II and III nicely reproduce the DFT-calculated band structures in Fig. 4 for ABC TLG and Fig. 16 for ABA TLG, employing the orbital model Hamiltonians,  $\mathcal{H}_{\text{orb}}^{\text{ABA}}$  and  $\mathcal{H}_{\text{orb}}^{\text{ABC}}$ , from the main text. The electric field behavior of the ABC TLG dispersion and DOS was already discussed in the main text. For the ABA TLG, the electric field also introduces a potential difference between the outermost layers, separating the monolayer graphene bands in energy. The BLG bands stay more or less the same with the applied field; see Fig. 16. In addition, a small band gap is introduced at the Fermi level. However, the gap first increases and then decreases again, when tuning the field from 0 to 1 V/nm. From the DOS, we find VHS associated with the parabolic BLG bands. With increasing field, we find that these

TABLE II. The fit parameters of the orbital model Hamiltonian  $\mathcal{H}_{\text{orb}}^{\text{ABA}}$  for ABA TLG with electric field. The fitted band structure results are summarized in Fig. 16.

Electric field (V/nm)	0	0.25	0.5	0.75	1.0
$\gamma_0$ (eV)	2.5692	2.5693	2.5695	2.5693	2.5688
$\gamma_1$ (eV)	0.3699	0.3700	0.3700	0.3700	0.3701
$\gamma_2$ (eV)	-0.0101	-0.0101	-0.0100	-0.0099	-0.0098
$\gamma_3$ (eV)	0.2829	0.2821	0.2798	0.2772	0.2742
$\gamma_4$ (eV)	-0.1643	-0.1640	-0.1638	-0.1642	-0.1635
$\gamma_5$ (eV)	0.0150	0.0130	0.0129	0.0130	0.0132
$V_1$ (meV)	0	-19.146	-38.608	-57.927	-78.221
$V_2$ (meV)	-19.991	-14.814	-13.980	-13.846	-14.715
$\Delta$ (meV)	20.566	24.193	24.452	24.158	23.983
$\eta$ (meV)	6.965	12.842	13.189	12.757	12.506
dipole (Debye)	0	0.0250	0.0499	0.0749	0.0996

TABLE III. The fit parameters of the orbital model Hamiltonian  $\mathcal{H}_{\text{orb}}^{\text{ABC}}$  for ABC TLG with electric field. The fitted band-structure results are summarized in Fig. 4.

Electric field (V/nm)	0	0.25	0.5	0.75	1.0
$\gamma_0$ (eV)	2.5539	2.5560	2.5656	2.5884	2.6198
$\gamma_1$ (eV)	0.3690	0.3689	0.3689	0.3687	0.3685
$\gamma_3$ (eV)	0.2917	0.2948	0.2960	0.2905	0.2816
$\gamma_4$ (eV)	-0.1646	-0.1642	-0.1618	-0.1571	-0.1516
$\gamma_6$ (eV)	0.0108	0.0113	0.0117	0.0115	0.0111
$V_1$ (meV)	0	-3.050	-10.124	-18.172	-25.409
$V_2$ (meV)	-37.243	-37.184	-36.066	-34.365	-32.529
$\Delta$ (meV)	10.288	9.746	9.001	9.816	9.094
$\eta$ (meV)	-1.121	-1.551	-1.664	0.172	0.467
dipole (Debye)	0	0.0286	0.0552	0.0812	0.1077

bands flatten even further near the Fermi level, which comes along with increasing VHS in the DOS.

The fitted electric field results, summarized in Tables II and III, are valuable for further theoretical considerations, e.g., gate-tunable transport simulations of bare ABA and ABC TLG. If one wants to add SOC, this can be easily done on a model level, employing the intrinsic SOC of bare graphene,  $\lambda_1 = 12 \mu\text{eV}$ , for all sublattice atoms [97,98]. The Rashba SOC would be even smaller (at maximum  $5 \mu\text{eV}$ ) for our investigated field values [69,99]. Certainly, one can also add proximity spin-orbit or exchange couplings, as we describe for our encapsulated structures.

## APPENDIX B: BARE ABB TRILAYER GRAPHENE

In addition to ABA and ABC TLG, there is also another stacking sequence, namely the ABB one. All those stackings are present in recent investigations on twisted-graphene/BLG heterostructures [83,93–95]. In the same manner as above and in the main text, we calculated the dispersion, DOS, and analyze the electric field behavior of ABB TLG. A reasonable orbital Hamiltonian for ABB TLG can be constructed by combining the knowledge about AA and AB stacked BLG together with the ABC and ABA TLG [69,99,138,139]. We propose the following ABB TLG orbital

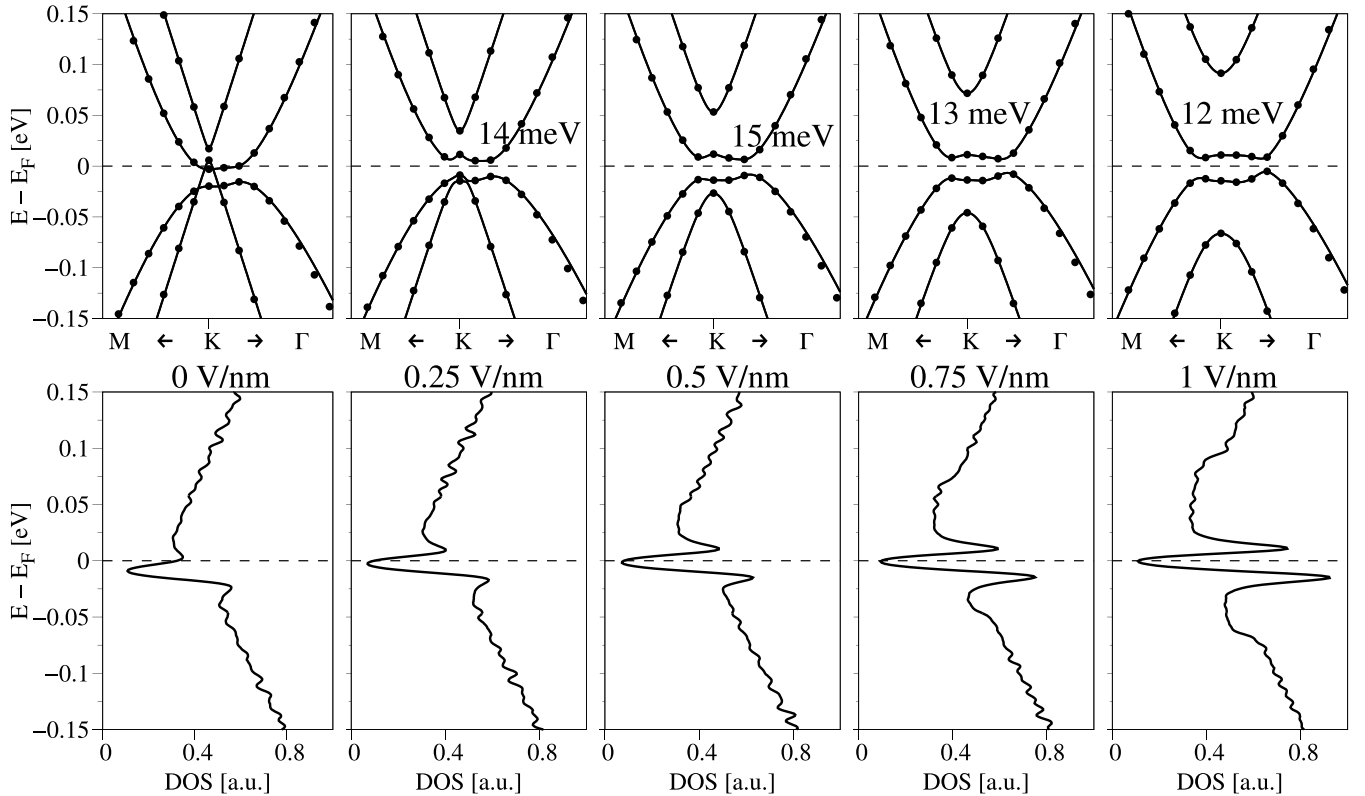


FIG. 16. Top: Zooms to the ABA TLG bands in the vicinity of the  $K$  point. We compare DFT data (symbols) with the model fits (solid lines) employing parameters from Table II. In the dispersion, we list the band gap at the Fermi level. Bottom: The corresponding calculated density of states (DOS). From left to right, we increase the transverse electric field from 0 to 1 V/nm.



Hamiltonian:

$$\mathcal{H}_{\text{orb}}^{\text{ABB}} = \begin{pmatrix} \Delta + V_1 & \gamma_0 f(\mathbf{k}) & \gamma_4 f^*(\mathbf{k}) & \gamma_1 & 0 & \gamma_5 \\ \gamma_0 f^*(\mathbf{k}) & V_1 & \gamma_3 f(\mathbf{k}) & \gamma_4 f^*(\mathbf{k}) & 0 & 0 \\ \gamma_4 f(\mathbf{k}) & \gamma_3 f^*(\mathbf{k}) & \Delta + V_2 & \gamma_0 f(\mathbf{k}) & \gamma_1' & \gamma_7 f(\mathbf{k}) \\ \gamma_1 & \gamma_4 f(\mathbf{k}) & \gamma_0 f^*(\mathbf{k}) & \Delta + V_2 & \gamma_7 f(\mathbf{k}) & \gamma_1' \\ 0 & 0 & \gamma_1' & \gamma_7 f^*(\mathbf{k}) & \Delta - V_1 & \gamma_0 f(\mathbf{k}) \\ \gamma_5 & 0 & \gamma_7 f^*(\mathbf{k}) & \gamma_1' & \gamma_0 f^*(\mathbf{k}) & \Delta - V_1 \end{pmatrix} \otimes s_0. \quad (\text{B1})$$

A schematic illustration of the couplings in ABB TLG is shown in Fig. 17. The hoppings between the bottom and middle graphene layer are the same as for the other TLG structures. However, the hoppings between the middle and the top graphene layer are adapted from the AA BLG structure [139]. Since the ABB TLG has no  $z$ -mirror or inversion symmetry connecting the top and bottom layer, the direct interlayer hoppings  $\gamma_1$  and  $\gamma_1'$  can in principle be different. Only when the interlayer distances are the same are the hopping amplitudes also the same. The coupling  $\gamma_7$ , connecting opposite sublattices from different layers, is similar to the coupling  $\gamma_4$ , connecting same sublattices from different layers. Nevertheless, they can be very different in amplitude.

The pseudospin character and the spin-orbit splittings in the bare ABB TLG dispersion have already been discussed in the main text. In Fig. 18, we show a zoom to the ABB TLG low-energy bands, further emphasizing the effect of a transverse electric field on the dispersion and the spin splittings. Applying the field apparently flips the low-energy band splittings at the  $K$  point with respect to the Fermi level. This is not surprising, considering the projected band structure in Fig. 3(c). Without the field, the low-energy conduction (valence) band has a pronounced contribution from  $B_1$  ( $B_3$ ) atoms near the anticrossing points away from  $K$ . With the electric field, applied along the positive  $z$  direction, a potential difference between the outermost layers is

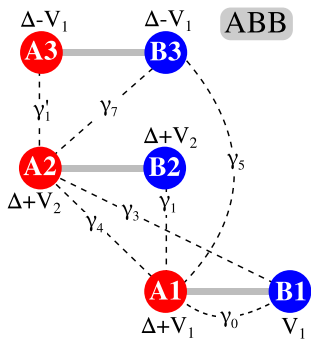


FIG. 17. Schematic illustration of the ABB TLG lattice, showing the relevant intra- and interlayer hoppings  $\gamma_j$ ,  $j = \{0, 1, 3, 4, 5, 7\}$  (dashed lines). In addition, the bottom (top) graphene layer is placed in the potential  $V_1$  ( $-V_1$ ), while the middle layer is placed in the potential  $V_2$ . The asymmetry  $\Delta$  arises due to vertical hoppings. In general, the direct interlayer couplings  $\gamma_1$  and  $\gamma_1'$  can be different. However, when both interlayer distances are the same (in our case fixed to  $d = 3.3$  Å),  $\gamma_1 = \gamma_1'$  holds.

introduced, such that the bottom layer is now in the lowest potential. Therefore, the band characters of valence and conduction bands flip, along with the spin splittings near the  $K$  point.

In Fig. 19, we summarize the electric field behavior of the band structure and DOS for the ABB TLG. The dispersion can be nicely reproduced by the orbital model Hamiltonian, employing the fit results from Table IV.

### APPENDIX C: EFFECTS OF RELAXATION ON BARE TLG DISPERSIONS

In the main text, when discussing bare TLG, we have fixed the interlayer distances between the graphene layers to  $d = 3.3$  Å, which is an approximation. We now allow the TLG structures to minimize their energy by relaxing the C atom positions. For the relaxation we employ DFT-D2 vdW corrections [130,131] and use a quasinewton algorithm based on the trust radius procedure. To determine the interlayer

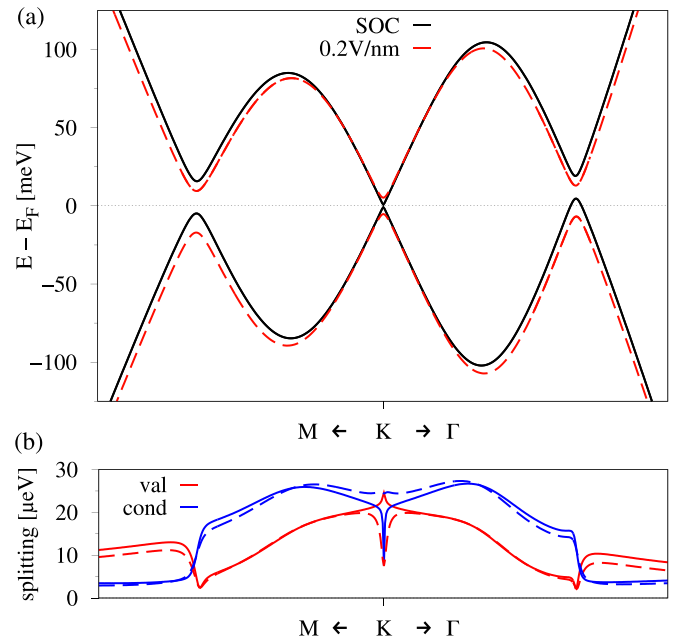


FIG. 18. (a) DFT-calculated low-energy bands of ABB TLG with SOC (black solid line) and additionally with a transverse electric field of 0.2 V/nm (red dashed line). (b) The spin splitting of valence (red) and conduction (blue) bands. Solid lines are with SOC only, and dashed lines are with SOC in the presence of the electric field.

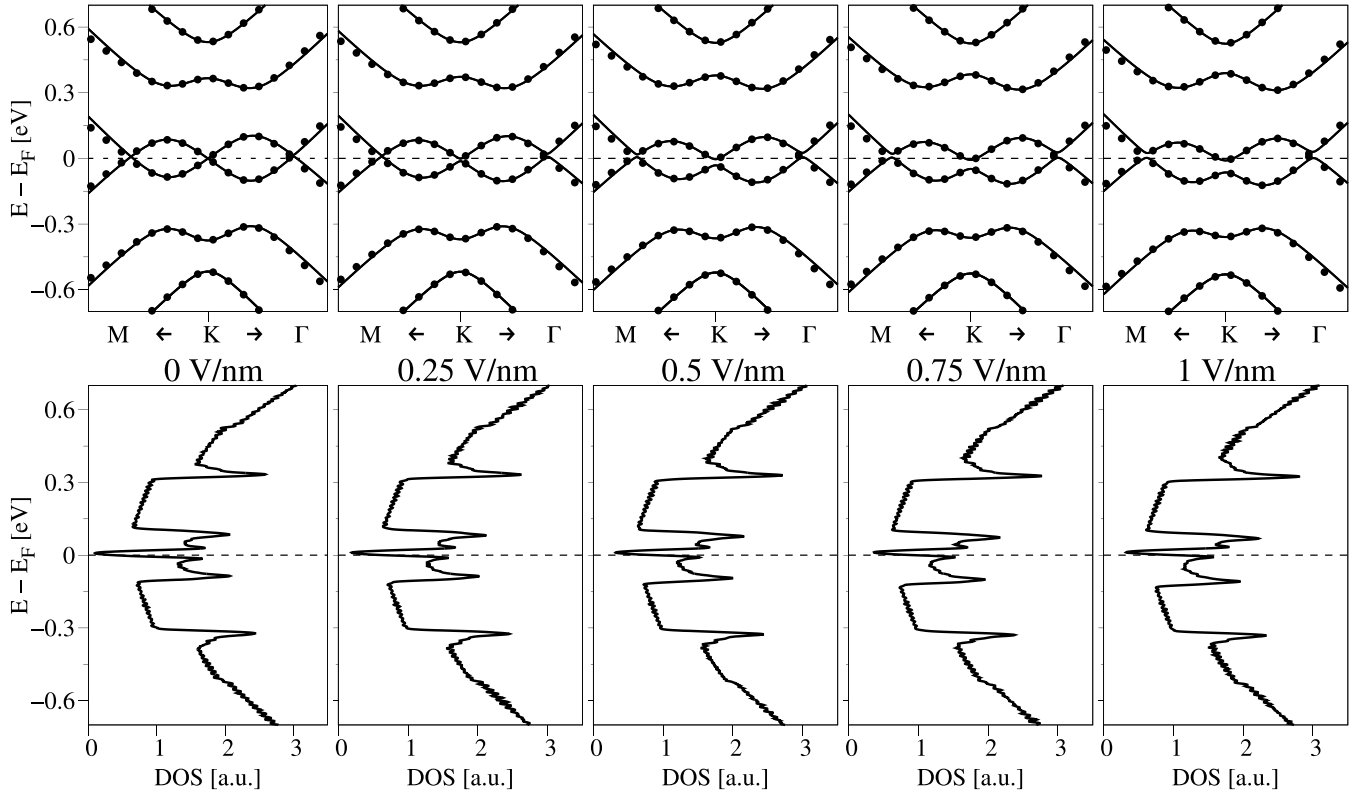


FIG. 19. Top: Zooms to the ABB TLG bands in the vicinity of the  $K$  point. We compare DFT data (symbols) with the model fits (solid lines) employing parameters from Table IV. Bottom: The corresponding calculated density of states (DOS). From left to right, we increase the transverse electric field from 0 to 1 V/nm.

distances, the carbon atoms are allowed to relax only in their  $z$  positions (vertical to the layers), until all components of all forces are reduced below  $10^{-4}$  (Ry/ $a_0$ ), where  $a_0$  is the Bohr radius.

After relaxation, interlayer distances are slightly reduced to about  $d = 3.24$  Å. The only exception is the interlayer distance between BB-layers in ABB TLG, which is relaxed to about  $d = 3.50$  Å. With the relaxed interlayer distances it is now also reasonable to compare the total energies of all the stackings. We find that the ABA TLG is energetically most favorable. However, the ABC one is only about 60  $\mu$ eV higher in energy. The ABB TLG is 25 meV higher in energy than the ABA one, making this stacking less favorable

to be observed naturally. In Fig. 20, we compare the band structure and DOS results for the TLG structures with and without the relaxation. The most drastic changes can be seen in the ABB TLG dispersion, since interlayer distances are now highly asymmetric. For the ABC and ABA TLG structures, the dispersion is barely different, except for the high-energy bands.

In Table V, we summarize the fit results when the structures are relaxed. In particular, the direct interlayer couplings  $\gamma_1$  and  $\gamma'_1$  are strongly renormalized because of the different interlayer distances. The high-energy bands are split off exactly due to these couplings, explaining the differences in the dispersions with and without relaxation.

TABLE IV. The fit parameters of the model Hamiltonian  $\mathcal{H}_{\text{orb}}^{\text{ABB}}$  for ABB TLG with electric field, assuming  $\gamma_1 = \gamma'_1$ . The fitted band-structure results are summarized in Fig. 19.

Electric field (V/nm)	0	0.25	0.5	0.75	1.0
$\gamma_0$ (eV)	2.5662	2.5682	2.5713	2.5737	2.5754
$\gamma_1$ (eV)	0.3698	0.3697	0.3693	0.3687	0.3683
$\gamma_3$ (eV)	0.2726	0.2723	0.2716	0.2706	0.2694
$\gamma_4$ (eV)	-0.1716	-0.1699	-0.1722	-0.1760	-0.1793
$\gamma_5$ (eV)	0.0229	0.0228	0.0246	0.0264	0.0275
$\gamma_7$ (eV)	-0.1087	-0.1101	-0.1053	-0.0966	-0.0874
$V_1$ (meV)	0	-12.982	-31.824	-48.449	-64.292
$V_2$ (meV)	-51.533	-53.755	-60.330	-66.823	-71.386
$\Delta$ (meV)	21.367	21.737	20.917	19.660	18.542
dipole (Debye)	0	0.0245	0.0500	0.0764	0.1029

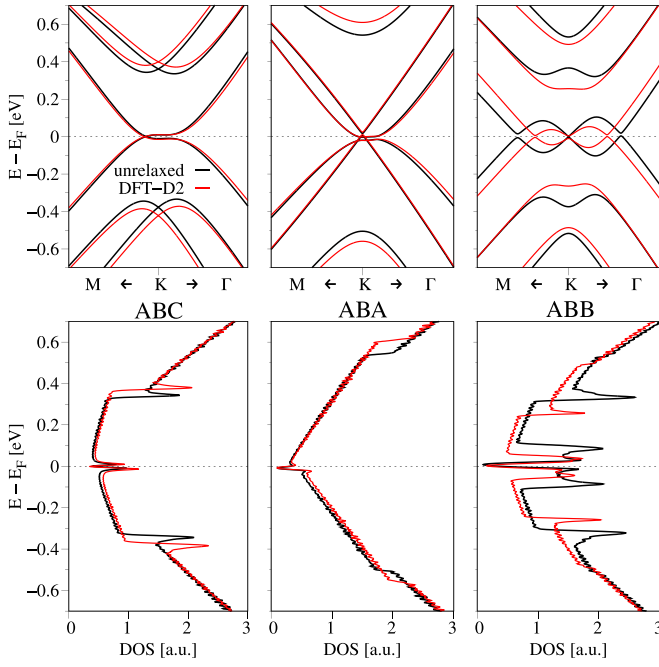


FIG. 20. Top: Zooms to the TLG dispersions in the vicinity of the  $K$  point. We compare unrelaxed (black) and fully relaxed (red) structures employing DFT-D2 vdW corrections. Bottom: The corresponding calculated density of states (DOS). The red lines can be reproduced (not shown) by model Hamiltonian parameters summarized in Table V.

TABLE V. The fit parameters of the model Hamiltonians for the relaxed TLG structures. The dispersions are shown in Fig. 20.

TLG	ABC	ABA	ABB
$\gamma_0$ (eV)	2.5470	2.5687	2.5845
$\gamma_1$ (eV)	0.4103	0.4128	0.4133
$\gamma'_1$ (eV)			0.2593
$\gamma_2$ (eV)		-0.0067	
$\gamma_3$ (eV)	0.3243	0.3128	0.2755
$\gamma_4$ (eV)	-0.1794	-0.1954	-0.2018
$\gamma_5$ (eV)		0.0089	0.0167
$\gamma_6$ (eV)	0.0133		
$\gamma_7$ (eV)			-0.0077
$V_1$ (meV)	0	0	0
$V_2$ (meV)	-45.161	-20.831	-27.767
$\Delta$ (meV)	11.105	31.501	9.040
$\eta$ (meV)	-2.838	5.069	

#### APPENDIX D: PSEUDOSPIN CHARACTER OF TMDC ENCAPSULATED TLG DISPERSIONS

In Fig. 21, we show the pseudospin character of the relevant ABA TLG bands of the TMDC encapsulated heterostructure. Similar to Fig. 1, the parabolic BLG-like bands are formed by atoms  $B_1$ ,  $A_2$ , and  $B_3$ , which form the nondimer interlayer pairs. The Dirac bands are formed by orbitals from the outermost graphene layers.

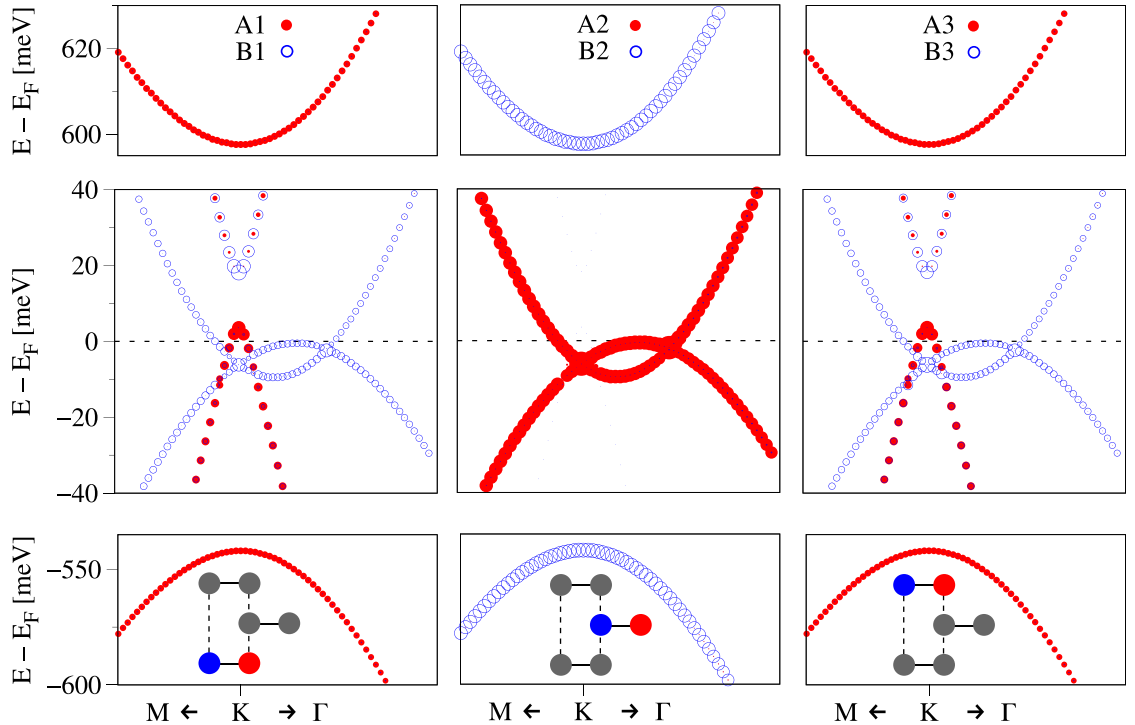


FIG. 21. Zooms to the TLG bands in the vicinity of the  $K$  point of the  $\text{MoSe}_2/\text{ABA-TLG}/\text{WS}_2$  heterostructure. From left to right, we project onto the sublattice atoms ( $A$  = red-filled circles,  $B$  = blue-open circles) of the bottom, middle, and top graphene layers. The sublattice atoms are indicated in the sketch of the ABA TLG geometry in the lower panels.

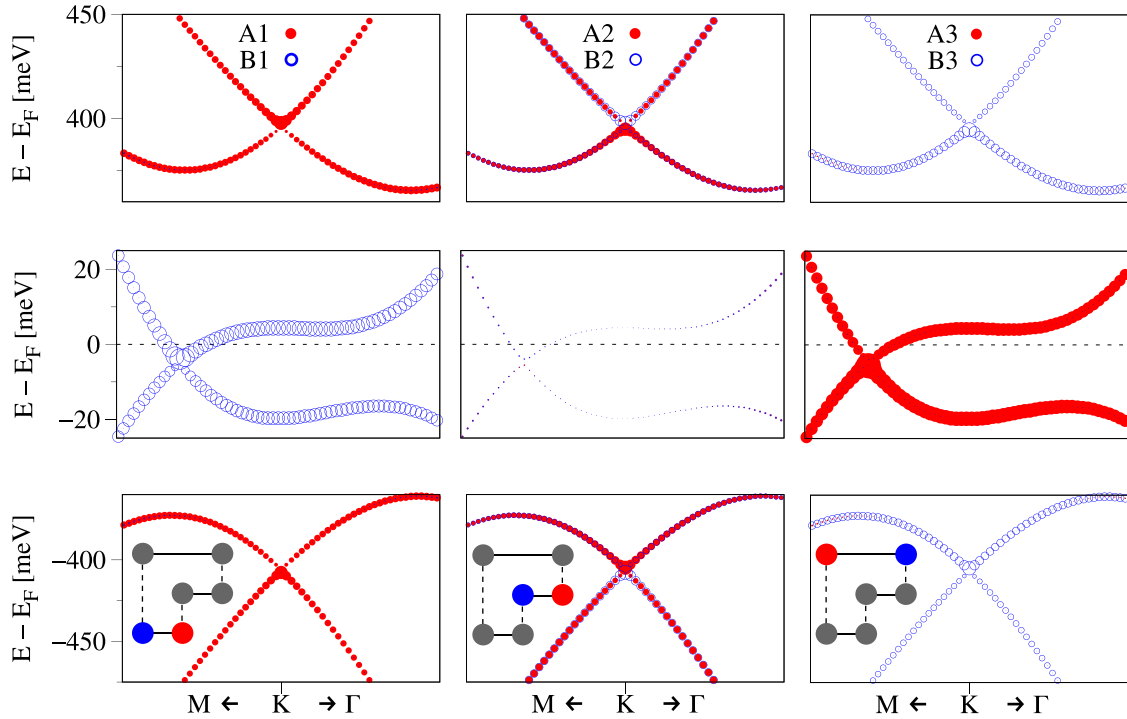


FIG. 22. ZOOMS to the TLG bands in the vicinity of the  $K$  point of the  $\text{MoSe}_2/\text{ABC-TLG}/\text{WSe}_2$  heterostructure. From left to right, we project onto the sublattice atoms ( $A$  = red-filled circles,  $B$  = blue-open circles) of the bottom, middle, and top graphene layers. The sublattice atoms are indicated in the sketch of the ABC TLG geometry in the lower panels.

In Fig. 22, we show the pseudospin character of the ABC TLG bands of the TMDC encapsulated heterostructure. Consistent with Fig. 2, the flat low-energy bands are formed by

the outer-layer atoms  $B_1$  and  $A_3$ , while high-energy bands are formed by all other atoms.

- [1] W. Han, R. K. Kawakami, M. Gmitra, and J. Fabian, Graphene spintronics, *Nat. Nanotechnol.* **9**, 794 (2014).
- [2] J. Fabian, A. Matos-Abiad, C. Ertler, P. Stano, and I. Zutic, Semiconductor spintronics, *Acta Phys. Slov.* **57**, 565 (2007).
- [3] C. Gong and X. Zhang, Two-dimensional magnetic crystals and emergent heterostructure devices, *Science* **363**, eaav4450 (2019).
- [4] H. Li, S. Ruan, and Yu-Jia Zeng, Intrinsic van der Waals magnetic materials from bulk to the 2D limit: New frontiers of spintronics, *Adv. Mater.* **31**, 1900065 (2019).
- [5] D. L. Cortie, G. L. Causer, K. C. Rule, H. Fritzsche, W. Kreuzpaintner, and F. Klose, Two-dimensional magnets: Forgotten history and recent progress towards spintronic applications, *Adv. Funct. Mater.* **30**, 1901414 (2019).
- [6] I. Zutic, A. Matos-Abiad, B. Scharf, H. Dery, and K. Belashchenko, Proximitized materials, *Mater. Today* **22**, 85 (2019).
- [7] J. F. Sierra, J. Fabian, R. K. Kawakami, S. Roche, and S. O. Valenzuela, Van der Waals heterostructures for spintronics and opto-spintronics, *Nat. Nanotechnol.* **16**, 856 (2021).
- [8] J. Li, H.-B. Leng, H. Fu, K. Watanabe, T. Taniguchi, X. Liu, C.-X. Liu, and J. Zhu, Superconducting proximity effect in a transparent van der Waals superconductor-metal junction, *Phys. Rev. B* **101**, 195405 (2020).
- [9] R. Moriya, N. Yabuki, and T. Machida, Superconducting proximity effect in a  $\text{NbSe}_2/\text{graphene}$  van der Waals junction, *Phys. Rev. B* **101**, 054503 (2020).
- [10] D. J. Trainer, B. K. Wang, F. Bobba, N. Samuelson, X. Xi, J. Zasadzinski, J. Nieminen, A. Bansil, and M. Iavarone, Proximity-induced superconductivity in monolayer  $\text{MoS}_2$ , *ACS Nano* **14**, 2718 (2020).
- [11] K. Zollner, M. Gmitra, T. Frank, and J. Fabian, Theory of proximity-induced exchange coupling in graphene on  $\text{hBN}/(\text{Co}, \text{Ni})$ , *Phys. Rev. B* **94**, 155441 (2016).
- [12] K. Zollner, M. Gmitra, and J. Fabian, Electrically tunable exchange splitting in bilayer graphene on monolayer  $\text{Cr}_2\text{X}_2\text{Te}_6$  with  $X = \text{Ge}, \text{Si}, \text{and Sn}$ , *New J. Phys.* **20**, 073007 (2018).
- [13] K. Zollner, P. E. Faria Junior, and J. Fabian, Proximity exchange effects in  $\text{MoSe}_2$  and  $\text{WSe}_2$  heterostructures with  $\text{CrI}_3$ : Twist angle, layer, and gate dependence, *Phys. Rev. B* **100**, 085128 (2019).
- [14] K. Zollner, P. E. Faria Junior, and J. Fabian, Giant proximity exchange and valley splitting in transition metal dichalcogenide/ $\text{hBN}/(\text{Co}, \text{Ni})$  heterostructures, *Phys. Rev. B* **101**, 085112 (2020).
- [15] J. Zhang, B. Zhao, Y. Yao, and Z. Yang, Robust quantum anomalous Hall effect in graphene-based van der Waals heterostructures, *Phys. Rev. B* **92**, 165418 (2015).



- [16] J. Zhang, B. Zhao, T. Zhou, Y. Xue, C. Ma, and Z. Yang, Strong magnetization and Chern insulators in compressed graphene/CrI<sub>3</sub> van der Waals heterostructures, *Phys. Rev. B* **97**, 085401 (2018).
- [17] M. Vila, J. H. Garcia, and S. Roche, Valley-polarized quantum anomalous Hall phase in bilayer graphene with layer-dependent proximity effects, *Phys. Rev. B* **104**, L161113 (2021).
- [18] Z. Wang, C. Tang, R. Sachs, Y. Barlas, and J. Shi, Proximity-Induced Ferromagnetism in Graphene Revealed by the Anomalous Hall Effect, *Phys. Rev. Lett.* **114**, 016603 (2015).
- [19] L. Xu, M. Yang, L. Shen, J. Zhou, T. Zhu, and Y. P. Feng, Large valley splitting in monolayer WS<sub>2</sub> by proximity coupling to an insulating antiferromagnetic substrate, *Phys. Rev. B* **97**, 041405(R) (2018).
- [20] H. X. Yang, A. Hallal, D. Terrade, X. Waintal, S. Roche, and M. Chshiev, Proximity Effects Induced in Graphene by Magnetic Insulators: First-Principles Calculations on Spin Filtering and Exchange-Splitting Gaps, *Phys. Rev. Lett.* **110**, 046603 (2013).
- [21] D. Zhong, K. L. Seyler, X. Linpeng, N. P. Wilson, T. Taniguchi, K. Watanabe, M. A. McGuire, K.-M. C. Fu, D. Xiao, W. Yao, and X. Xu, Layer-resolved magnetic proximity effect in van der Waals heterostructures, *Nat. Nanotechnol.* **15**, 187 (2020).
- [22] D. V. Averyanov, I. S. Sokolov, A. M. Tokmachev, O. E. Parfenov, I. A. Karateev, A. N. Taldenkov, and V. G. Storchak, High-temperature magnetism in graphene induced by proximity to EuO, *ACS Appl. Mater. Interfaces* **10**, 20767 (2018).
- [23] L. Ciorciaro, M. Kroner, K. Watanabe, T. Taniguchi, and A. Imamoglu, Observation of Magnetic Proximity Effect Using Resonant Optical Spectroscopy of an Electrically Tunable MoSe<sub>2</sub>/CrBr<sub>3</sub> Heterostructure, *Phys. Rev. Lett.* **124**, 197401 (2020).
- [24] M. Gmitra and J. Fabian, Graphene on transition-metal dichalcogenides: A platform for proximity spin-orbit physics and optospintronics, *Phys. Rev. B* **92**, 155403 (2015).
- [25] M. Gmitra, D. Kochan, P. Högl, and J. Fabian, Trivial and inverted Dirac bands and the emergence of quantum spin Hall states in graphene on transition-metal dichalcogenides, *Phys. Rev. B* **93**, 155104 (2016).
- [26] K. Zollner and J. Fabian, Single and bilayer graphene on the topological insulator Bi<sub>2</sub>Se<sub>3</sub>: Electronic and spin-orbit properties from first principles, *Phys. Rev. B* **100**, 165141 (2019).
- [27] K. Zollner and J. Fabian, Heterostructures of graphene and topological insulators Bi<sub>2</sub>Se<sub>3</sub>, Bi<sub>2</sub>Te<sub>3</sub>, and Sb<sub>2</sub>Te<sub>3</sub>, *Phys. Status Solidi B* **258**, 2000081 (2021).
- [28] K. Song, D. Soriano, A. W. Cummings, R. Robles, P. Ordejón, and S. Roche, Spin proximity effects in graphene/topological insulator heterostructures, *Nano Lett.* **18**, 2033 (2018).
- [29] J. Zhang, C. Triola, and E. Rossi, Proximity Effect in Graphene-Topological-Insulator Heterostructures, *Phys. Rev. Lett.* **112**, 096802 (2014).
- [30] A. Avsar, D. Unuchek, J. Liu, O. L. Sanchez, K. Watanabe, T. Taniguchi, B. Özyilmaz, and A. Kis, Optospintronics in graphene via proximity coupling, *ACS Nano* **11**, 11678 (2017).
- [31] A. Avsar, J. Y. Tan, T. Taychatanapat, J. Balakrishnan, G. K. W. Koon, Y. Yeo, J. Lahiri, A. Carvalho, A. S. Rodin, E. C. T. O'Farrell, G. Eda, A. H. Castro Neto, and B. Özyilmaz, Spin-orbit proximity effect in graphene, *Nat. Commun.* **5**, 4875 (2014).
- [32] A. M. Alsharari, M. M. Asmar, and S. E. Ulloa, Proximity-induced topological phases in bilayer graphene, *Phys. Rev. B* **97**, 241104(R) (2018).
- [33] T. Frank, M. Gmitra, and J. Fabian, Theory of electronic and spin-orbit proximity effects in graphene on Cu(111), *Phys. Rev. B* **93**, 155142 (2016).
- [34] A. David, P. Rakya, A. Kormányos, and G. Burkard, Induced spin-orbit coupling in twisted graphene-transition metal dichalcogenide heterobilayers: Twistronics meets spintronics, *Phys. Rev. B* **100**, 085412 (2019).
- [35] T. S. Ghiasi, A. A. Kaverzin, P. J. Blah, and B. J. van Wees, Charge-to-Spin Conversion by the Rashba-Edelstein Effect in Two-Dimensional van der Waals Heterostructures up to Room Temperature, *Nano Lett.* **19**, 5959 (2019).
- [36] L. A. Benitez, W. S. Torres, J. F. Sierra, M. Timmermans, J. H. Garcia, S. Roche, M. V. Costache, and S. O. Valenzuela, Tunable room-temperature spin galvanic and spin Hall effects in van der Waals heterostructures, *Nat. Mater.* **19**, 170 (2020).
- [37] Y. K. Luo, J. Xu, T. Zhu, G. Wu, E. J. McCormick, W. Zhan, M. R. Neupane, and R. K. Kawakami, Opto-valleytronic spin injection in monolayer MoS<sub>2</sub>/few-layer graphene hybrid spin valves, *Nano Lett.* **17**, 3877 (2017).
- [38] C. Safeer, J. Ingla-Aynés, F. Herling, J. H. Garcia, M. Vila, N. Ontoso, M. R. Calvo, S. Roche, L. E. Hueso, and F. Casanova, Room-temperature spin Hall effect in graphene/MoS<sub>2</sub> van der Waals heterostructures, *Nano Lett.* **19**, 1074 (2019).
- [39] F. Herling, C. K. Safeer, J. Ingla-Aynés, N. Ontoso, L. E. Hueso, and F. Casanova, Gate tunability of highly efficient spin-to-charge conversion by spin hall effect in graphene proximitized with WSe<sub>2</sub>, *APL Mater.* **8**, 071103 (2020).
- [40] K. Zollner and J. Fabian, Engineering Proximity Exchange by Twisting: Reversal of Ferromagnetic and Emergence of Antiferromagnetic Dirac Bands in Graphene/Cr<sub>2</sub>Ge<sub>2</sub>Te<sub>6</sub>, *Phys. Rev. Lett.* **128**, 106401 (2022).
- [41] T. Naimier, K. Zollner, M. Gmitra, and J. Fabian, Twist-angle dependent proximity induced spin-orbit coupling in graphene/transition metal dichalcogenide heterostructures, *Phys. Rev. B* **104**, 195156 (2021).
- [42] S. Carr, D. Massatt, S. Fang, P. Cazeaux, M. Luskin, and E. Kaxiras, Twistronics: Manipulating the electronic properties of two-dimensional layered structures through their twist angle, *Phys. Rev. B* **95**, 075420 (2017).
- [43] Z. Hennighausen and S. Kar, Twistronics: A turning point in 2d quantum materials, *Electron. Struct.* **3**, 014004 (2021).
- [44] R. Ribeiro-Palau, C. Zhang, K. Watanabe, T. Taniguchi, J. Hone, and C. R. Dean, Twistable electronics with dynamically rotatable heterostructures, *Science* **361**, 690 (2018).
- [45] S. Carr, S. Fang, and E. Kaxiras, Electronic-structure methods for twisted moiré layers, *Nat. Rev. Mater.* **5**, 748 (2020).
- [46] Y. Cao, V. Fatemi, S. Fang, K. Watanabe, T. Taniguchi, E. Kaxiras, and P. Jarillo-Herrero, Unconventional superconductivity in magic-angle graphene superlattices, *Nature (London)* **556**, 43 (2018).
- [47] Y. Cao, V. Fatemi, A. Demir, S. Fang, S. L. Tomarken, J. Y. Luo, J. D. Sanchez-Yamagishi, K. Watanabe, T. Taniguchi, E. Kaxiras, R. C. Ashoori, and P. Jarillo-Herrero, Correlated

- insulator behaviour at half-filling in magic-angle graphene superlattices, *Nature (London)* **556**, 80 (2018).
- [48] H. S. Arora, R. Polski, Y. Zhang, A. Thomson, Y. Choi, H. Kim, Z. Lin, I. Z. Wilson, X. Xu, J.-H. Chu *et al.*, Superconductivity in metallic twisted bilayer graphene stabilized by  $\text{WSe}_2$ , *Nature (London)* **583**, 379 (2020).
- [49] P. Stepanov, I. Das, X. Lu, A. Fahimniya, K. Watanabe, T. Taniguchi, F. H. L. Koppens, J. Lischner, L. Levitov, and D. K. Efetov, Untying the insulating and superconducting orders in magic-angle graphene, *Nature (London)* **583**, 375 (2020).
- [50] X. Lu, P. Stepanov, W. Yang, M. Xie, M. A. Aamir, I. Das, C. Urgell, K. Watanabe, T. Taniguchi, G. Zhang *et al.*, Superconductors, orbital magnets and correlated states in magic-angle bilayer graphene, *Nature (London)* **574**, 653 (2019).
- [51] A. L. Sharpe, E. J. Fox, A. W. Barnard, J. Finney, K. Watanabe, T. Taniguchi, M. A. Kastner, and D. Goldhaber-Gordon, Emergent ferromagnetism near three-quarters filling in twisted bilayer graphene, *Science* **365**, 605 (2019).
- [52] M. Gmitra and J. Fabian, Proximity effects in bilayer graphene on monolayer  $\text{WSe}_2$ : Field-Effect Spin Valley Locking, Spin-Orbit Valve, and Spin Transistor, *Phys. Rev. Lett.* **119**, 146401 (2017).
- [53] J. Amann, T. Völkl, T. Rockinger, D. Kochan, K. Watanabe, T. Taniguchi, J. Fabian, D. Weiss, and J. Eroms, Counterintuitive gate dependence of weak antilocalization in bilayer graphene/ $\text{WSe}_2$  heterostructures, *arXiv:2012.05718*.
- [54] K. Zollner, M. Gmitra, and J. Fabian, Swapping Exchange and Spin-Orbit Coupling in 2D Van der Waals Heterostructures, *Phys. Rev. Lett.* **125**, 196402 (2020).
- [55] J.-X. Lin, Y.-H. Zhang, E. Morissette, Z. Wang, S. Liu, D. Rhodes, K. Watanabe, T. Taniguchi, J. Hone, and J. I. A. Li, Spin-orbit driven ferromagnetism at half moiré filling in magic-angle twisted bilayer graphene, *Science* **375**, 437 (2022).
- [56] D. Wang, S. Che, G. Cao, R. Lyu, K. Watanabe, T. Taniguchi, C. N. Lau, and M. Bockrath, Quantum Hall Effect Measurement of Spin-Orbit Coupling Strengths in Ultraclean Bilayer Graphene/ $\text{WSe}_2$  Heterostructures, *Nano Lett.* **19**, 7028 (2019).
- [57] J. O. Island, X. Cui, C. Lewandowski, J. Y. Khoo, E. M. Spanton, H. Zhou, D. Rhodes, J. C. Hone, T. Taniguchi, K. Watanabe, L. S. Levitov, M. P. Zaletel, and A. F. Young, Spin-orbit-driven band inversion in bilayer graphene by the van der Waals proximity effect, *Nature (London)* **571**, 85 (2019).
- [58] C. Cardoso, D. Soriano, N. A. García-Martínez, and J. Fernández-Rossier, Van der Waals Spin Valves, *Phys. Rev. Lett.* **121**, 067701 (2018).
- [59] P. Tiwari, S. K. Srivastav, and A. Bid, Electric-Field-Tunable Valley Zeeman Effect in Bilayer Graphene Heterostructures: Realization of the Spin-Orbit Valve Effect, *Phys. Rev. Lett.* **126**, 096801 (2021).
- [60] K. Zollner and J. Fabian, Bilayer graphene encapsulated within monolayers of  $\text{WS}_2$  or  $\text{Cr}_2\text{Ge}_2\text{Te}_6$ : Tunable proximity spin-orbit or exchange coupling, *Phys. Rev. B* **104**, 075126 (2021).
- [61] R. Bistritzer and A. H. MacDonald, Moiré bands in twisted double-layer graphene, *Proc. Natl. Acad. Sci. USA* **108**, 12233 (2011).
- [62] A. Nimbalkar and H. Kim, Opportunities and challenges in twisted bilayer graphene: A review, *Nano-Micro Lett.* **12**, 126 (2020).
- [63] Y. Saito, J. Ge, K. Watanabe, T. Taniguchi, and A. F. Young, Independent superconductors and correlated insulators in twisted bilayer graphene, *Nat. Phys.* **16**, 926 (2020).
- [64] C. Shen, Y. Chu, Q. S. Wu, N. Li, S. Wang, Y. Zhao, J. Tang, J. Liu, J. Tian, K. Watanabe *et al.*, Correlated states in twisted double bilayer graphene, *Nat. Phys.* **16**, 520 (2020).
- [65] X. Liu, Z. Hao, E. Khalaf, J. Y. Lee, Y. Ronen, H. Yoo, D. H. Najafabadi, K. Watanabe, T. Taniguchi, A. Vishwanath *et al.*, Tunable spin-polarized correlated states in twisted double bilayer graphene, *Nature (London)* **583**, 221 (2020).
- [66] Y. Cao, D. Rodan-Legrain, O. Rubies-Bigorda, J. M. Park, K. Watanabe, T. Taniguchi, and P. Jarillo-Herrero, Tunable correlated states and spin-polarized phases in twisted bilayer-bilayer graphene, *Nature (London)* **583**, 215 (2020).
- [67] G. W. Burg, J. Zhu, T. Taniguchi, K. Watanabe, A. H. MacDonald, and E. Tutuc, Correlated Insulating States in Twisted Double Bilayer Graphene, *Phys. Rev. Lett.* **123**, 197702 (2019).
- [68] M. Serlin, C. L. Tschirhart, H. Polshyn, Y. Zhang, J. Zhu, K. Watanabe, T. Taniguchi, L. Balents, and A. F. Young, Intrinsic quantized anomalous Hall effect in a moiré heterostructure, *Science* **367**, 900 (2020).
- [69] S. Konschuh, Spin-orbit coupling effects: From graphene to graphite, Ph.D. thesis, University of Regensburg, 2011.
- [70] A. Kormányos and G. Burkard, Intrinsic and substrate induced spin-orbit interaction in chirally stacked trilayer graphene, *Phys. Rev. B* **87**, 045419 (2013).
- [71] S. H. Jhang, M. F. Craciun, S. Schmidmeier, S. Tokumitsu, S. Russo, M. Yamamoto, Y. Skourski, J. Wosnitza, S. Tarucha, J. Eroms, and C. Strunk, Stacking-order dependent transport properties of trilayer graphene, *Phys. Rev. B* **84**, 161408(R) (2011).
- [72] B. Ghosh and S. Misra, Monte carlo simulation study of spin transport in trilayer graphene: A comparison between ABA and ABC stacking, *J. Appl. Phys.* **112**, 073720 (2012).
- [73] Z. Chen, H. Yuan, Y. Zhang, K. Nomura, T. Gao, Y. Gao, H. Shimotani, Z. Liu, and Y. Iwasa, Tunable spin-orbit interaction in trilayer graphene exemplified in electric-double-layer transistors, *Nano Lett.* **12**, 2212 (2012).
- [74] M. U. Rehman and A. A. Abid, Quantum spin Hall and quantum valley Hall effects in trilayer graphene and their topological structures, *Chin. Phys. B* **26**, 127304 (2017).
- [75] Z. Ge, S. Slizovskiy, F. Joucken, E. A. Quezada, T. Taniguchi, K. Watanabe, V. I. Fal'ko, and J. Velasco, Control of Giant Topological Magnetic Moment and Valley Splitting in Trilayer Graphene, *Phys. Rev. Lett.* **127**, 136402 (2021).
- [76] R. Guerrero-Avilés, M. Pelc, F. Geisenhof, T. Weitz, and A. Ayuela, Relative stability of bernal and rhombohedral stackings in trilayer graphene under distortions, *arXiv:2110.06590*.
- [77] Z. Zhu, S. Carr, D. Massatt, M. Luskin, and E. Kaxiras, Twisted Trilayer Graphene: A Precisely Tunable Platform for Correlated Electrons, *Phys. Rev. Lett.* **125**, 116404 (2020).
- [78] J. M. Park, Y. Cao, K. Watanabe, T. Taniguchi, and P. Jarillo-Herrero, Tunable strongly coupled superconductivity in magic-angle twisted trilayer graphene, *Nature (London)* **590**, 249 (2021).
- [79] G. Chen, L. Jiang, S. Wu, B. Lyu, H. Li, B. L. Chittari, K. Watanabe, T. Taniguchi, Z. Shi, J. Jung *et al.*, Evidence of a gate-tunable Mott insulator in a trilayer graphene moiré superlattice, *Nat. Phys.* **15**, 237 (2019).

- [80] G. Chen, A. L. Sharpe, E. J. Fox, Y.-H. Zhang, S. Wang, L. Jiang, B. Lyu, H. Li, K. Watanabe, T. Taniguchi *et al.*, Tunable correlated chern insulator and ferromagnetism in a moiré superlattice, *Nature (London)* **579**, 56 (2020).
- [81] G. Chen, A. L. Sharpe, P. Gallagher, I. T. Rosen, E. J. Fox, L. Jiang, B. Lyu, H. Li, K. Watanabe, T. Taniguchi *et al.*, Signatures of tunable superconductivity in a trilayer graphene moiré superlattice, *Nature (London)* **572**, 215 (2019).
- [82] H. Zhou, T. Xie, A. Ghazaryan, T. Holder, J. R. Ehrets, E. M. Spanton, T. Taniguchi, K. Watanabe, E. Berg, M. Serbyn *et al.*, Half- and quarter-metals in rhombohedral trilayer graphene, *Nature (London)* **598**, 429 (2021).
- [83] H. Polshyn, J. Zhu, M. A. Kumar, Y. Zhang, F. Yang, C. L. Tschirhart, M. Serlin, K. Watanabe, T. Taniguchi, A. H. MacDonald *et al.*, Electrical switching of magnetic order in an orbital Chern insulator, *Nature (London)* **588**, 66 (2020).
- [84] V. T. Phong, P. A. Pantaleón, T. Cea, and F. Guinea, Band structure and superconductivity in twisted trilayer graphene, *Phys. Rev. B* **104**, L121116 (2021).
- [85] H. Zhou, T. Xie, T. Taniguchi, K. Watanabe, and A. F. Young, Superconductivity in rhombohedral trilayer graphene, *Nature (London)* **598**, 434 (2021).
- [86] W. Qin and A. H. MacDonald, In-Plane Critical Magnetic Fields in Magic-Angle Twisted Trilayer Graphene, *Phys. Rev. Lett.* **127**, 097001 (2021).
- [87] Y. Cao, J. M. Park, K. Watanabe, T. Taniguchi, and P. Jarillo-Herrero, Pauli-limit violation and re-entrant superconductivity in moiré graphene, *Nature (London)* **595**, 526 (2021).
- [88] Y.-Z. Chou, F. Wu, J. D. Sau, and S. Das Sarma, Acoustic-Phonon-Mediated Superconductivity in Rhombohedral Trilayer Graphene, *Phys. Rev. Lett.* **127**, 187001 (2021).
- [89] P. Siriviboon, J.-X. Lin, H. D. Scammell, S. Liu, D. Rhodes, K. Watanabe, T. Taniguchi, J. Hone, M. S. Scheurer, and J. I. A. Li, Abundance of density wave phases in twisted trilayer graphene on WSe<sub>2</sub>, *arXiv:2112.07127*.
- [90] J.-X. Lin, P. Siriviboon, H. D. Scammell, S. Liu, D. Rhodes, K. Watanabe, T. Taniguchi, J. Hone, M. S. Scheurer, and J. I. A. Li, Zero-field superconducting diode effect in twisted trilayer graphene, *arXiv:2112.07841*.
- [91] H. D. Scammell, J. I. A. Li, and M. S. Scheurer, Theory of zero-field diode effect in twisted trilayer graphene, *arXiv:2112.09115*.
- [92] The acronym “ex-so-tic” accounts for heterostructures with both proximity-induced spin interactions, exchange (ex) and spin-orbit (so) coupling.
- [93] L. Rademaker, I. V. Protopopov, and D. A. Abanin, Topological flat bands and correlated states in twisted monolayer-bilayer graphene, *Phys. Rev. Res.* **2**, 033150 (2020).
- [94] Y. Park, B. L. Chittari, and J. Jung, Gate-tunable topological flat bands in twisted monolayer-bilayer graphene, *Phys. Rev. B* **102**, 035411 (2020).
- [95] Z. Ma, S. Li, Y.-W. Zheng, M.-M. Xiao, H. Jiang, J.-H. Gao, and X. C. Xie, Topological flat bands in twisted trilayer graphene, *Sci. Bull.* **66**, 18 (2021).
- [96] P. Blaha, K. Schwarz, G. K. H. Madsen, D. Kvasnicka, and J. Luitz, *WIEN2K, An Augmented Plane Wave + Local Orbitals Program for Calculating Crystal Properties* (Vienna University of Technology, Institute of Materials Chemistry, 2001).
- [97] M. Gmitra, S. Konschuh, C. Ertler, C. Ambrosch-Draxl, and J. Fabian, Band-structure topologies of graphene: Spin-orbit coupling effects from first principles, *Phys. Rev. B* **80**, 235431 (2009).
- [98] S. Konschuh, M. Gmitra, and J. Fabian, Tight-binding theory of the spin-orbit coupling in graphene, *Phys. Rev. B* **82**, 245412 (2010).
- [99] S. Konschuh, M. Gmitra, D. Kochan, and J. Fabian, Theory of spin-orbit coupling in bilayer graphene, *Phys. Rev. B* **85**, 115423 (2012).
- [100] J. Sichau, M. Prada, T. Anlauf, T. J. Lyon, B. Bosnjak, L. Tiemann, and R. H. Blick, Resonance Microwave Measurements of an Intrinsic Spin-Orbit Coupling Gap in Graphene: A Possible Indication of a Topological State, *Phys. Rev. Lett.* **122**, 046403 (2019).
- [101] L. Banszerus, B. Frohn, T. Fabian, S. Somanchi, A. Epping, M. Müller, D. Neumaier, K. Watanabe, T. Taniguchi, F. Libisch, B. Beschoten, F. Hassler, and C. Stampfer, Observation of the Spin-Orbit Gap in Bilayer Graphene by One-Dimensional Ballistic Transport, *Phys. Rev. Lett.* **124**, 177701 (2020).
- [102] J. P. Perdew, K. Burke, and M. Ernzerhof, Generalized Gradient Approximation Made Simple, *Phys. Rev. Lett.* **77**, 3865 (1996).
- [103] S. Grimme, J. Antony, S. Ehrlich, and H. Krieg, A consistent and accurate ab initio parametrization of density functional dispersion correction (DFT-D) for the 94 elements H-Pu, *J. Chem. Phys.* **132**, 154104 (2010).
- [104] B. Partoens and F. M. Peeters, From graphene to graphite: Electronic structure around the  $k$  point, *Phys. Rev. B* **74**, 075404 (2006).
- [105] S. Latil and L. Henrard, Charge carriers in few-layer graphene films, *Phys. Rev. Lett.* **97**, 036803 (2006).
- [106] M. Koshino and E. McCann, Gate-induced interlayer asymmetry in aba-stacked trilayer graphene, *Phys. Rev. B* **79**, 125443 (2009).
- [107] M. Aoki and H. Amawashi, Dependence of band structures on stacking and field in layered graphene, *Solid State Commun.* **142**, 123 (2007).
- [108] M. Koshino and E. McCann, Trigonal warping and Berry’s phase  $n\pi$  in abc-stacked multilayer graphene, *Phys. Rev. B* **80**, 165409 (2009).
- [109] F. Zhang, B. Sahu, H. Min, and A. H. MacDonald, Band structure of *abc*-stacked graphene trilayers, *Phys. Rev. B* **82**, 035409 (2010).
- [110] C.-L. Lu, H.-C. Lin, C.-C. Hwang, J. Wang, M.-F. Lin, and C.-P. Chang, Absorption spectra of trilayer rhombohedral graphite, *Appl. Phys. Lett.* **89**, 221910 (2006).
- [111] J. C. Leutenantsmeyer, J. Ingla-Aynés, J. Fabian, and B. J. van Wees, Observation of Spin-Valley-Coupling-Induced Large Spin-Lifetime Anisotropy in Bilayer Graphene, *Phys. Rev. Lett.* **121**, 127702 (2018).
- [112] C. Mouldsdales, A. Knothe, and V. Fal’ko, Engineering of the topological magnetic moment of electrons in bilayer graphene using strain and electrical bias, *Phys. Rev. B* **101**, 085118 (2020).
- [113] Y. Lee, A. Knothe, H. Overweg, M. Eich, C. Gold, A. Kurzman, V. Klasovika, T. Taniguchi, K. Watanabe, V. Fal’ko, T. Ihn, K. Ensslin, and P. Rickhaus, Tunable Valley Splitting Due to Topological Orbital Magnetic Moment in Bilayer Graphene Quantum Point Contacts, *Phys. Rev. Lett.* **124**, 126802 (2020).

- [114] W. J. Schutte, J. L. De Boer, and F. Jellinek, Crystal structures of tungsten disulfide and diselenide, *J. Solid State Chem.* **70**, 207 (1987).
- [115] P. B. James and M. T. Lavik, The crystal structure of MoSe<sub>2</sub>, *Acta Cryst.* **16**, 1183 (1963).
- [116] K. Zollner, P. E. Faria Junior, and J. Fabian, Strain-tunable orbital, spin-orbit, and optical properties of monolayer transition-metal dichalcogenides, *Phys. Rev. B* **100**, 195126 (2019).
- [117] C. Si, Z. Sun, and F. Liu, Strain engineering of graphene: A review, *Nanoscale* **8**, 3207 (2016).
- [118] S.-M. Choi, S.-H. Jhi, and Y.-W. Son, Effects of strain on electronic properties of graphene, *Phys. Rev. B* **81**, 081407(R) (2010).
- [119] Y. Li and M. Koshino, Twist-angle dependence of the proximity spin-orbit coupling in graphene on transition-metal dichalcogenides, *Phys. Rev. B* **99**, 075438 (2019).
- [120] V. Carteaux, D. Brunet, G. Ouvrard, and G. Andre, Crystallographic, magnetic and electronic structures of a new layered ferromagnetic compound Cr<sub>2</sub>Ge<sub>2</sub>Te<sub>6</sub>, *J. Phys.: Condens. Matter* **7**, 69 (1995).
- [121] X. Li and J. Yang, CrXTe<sub>3</sub> (X = Si, Ge) nanosheets: Two dimensional intrinsic ferromagnetic semiconductors, *J. Mater. Chem. C* **2**, 7071 (2014).
- [122] X. Chen, J. Qi, and D. Shi, Strain-engineering of magnetic coupling in two-dimensional magnetic semiconductor CrSiTe<sub>3</sub>: Competition of direct exchange interaction and superexchange interaction, *Phys. Lett. A* **379**, 60 (2015).
- [123] L. Liu, X. Hu, Y. Wang, A. V. Krashennnikov, Z. Chen, and L. Sun, Tunable electronic properties and enhanced ferromagnetism in Cr<sub>2</sub>Ge<sub>2</sub>Te<sub>6</sub> monolayer by strain engineering, *Nanotechnology* **32**, 485408 (2021).
- [124] S. R. Bahn and K. W. Jacobsen, An object-oriented scripting interface to a legacy electronic structure code, *Comput. Sci. Eng.* **4**, 56 (2002).
- [125] K. Momma and F. Izumi, VESTA3 for three-dimensional visualization of crystal, volumetric and morphology data, *J. Appl. Cryst.* **44**, 1272 (2011).
- [126] P. Hohenberg and W. Kohn, Inhomogeneous Electron Gas, *Phys. Rev.* **136**, B864 (1964).
- [127] P. Giannozzi, S. Baroni, N. Bonini, M. Calandra, R. Car, C. Cavazzoni, D. Ceresoli, G. L. Chiarotti, M. Cococcioni, I. Dabo, A. D. Corso, S. de Gironcoli, S. Fabris, G. Fratesi, R. Gebauer, U. Gerstmann, C. Gougoussis, A. Kokalj, M. Lazzeri, L. Martin-Samos *et al.*, QUANTUM ESPRESSO: A modular and open-source software project for quantum simulations of materials, *J. Phys.: Condens. Matter* **21**, 395502 (2009).
- [128] G. Kresse and D. Joubert, From ultrasoft pseudopotentials to the projector augmented-wave method, *Phys. Rev. B* **59**, 1758 (1999).
- [129] C. Gong, L. Li, Z. Li, H. Ji, A. Stern, Y. Xia, T. Cao, W. Bao, C. Wang, Y. Wang, Z. Q. Qiu, R. J. Cava, S. G. Louie, J. Xia, and X. Zhang, Discovery of intrinsic ferromagnetism in two-dimensional van der Waals crystals, *Nature (London)* **546**, 265 (2017).
- [130] S. Grimme, Semiempirical GGA-type density functional constructed with a long-range dispersion correction, *J. Comput. Chem.* **27**, 1787 (2006).
- [131] V. Barone, M. Casarin, D. Forrer, M. Pavone, M. Sami, and A. Vittadini, Role and effective treatment of dispersive forces in materials: Polyethylene and graphite crystals as test cases, *J. Comput. Chem.* **30**, 934 (2009).
- [132] L. Bengtsson, Dipole correction for surface supercell calculations, *Phys. Rev. B* **59**, 12301 (1999).
- [133] M. Koshino, Interlayer screening effect in graphene multilayers with *aba* and *abc* stacking, *Phys. Rev. B* **81**, 125304 (2010).
- [134] Y.-C. Zhou, H.-L. Zhang, and W.-Q. Deng, A 3n rule for the electronic properties of doped graphene, *Nanotechnology* **24**, 225705 (2013).
- [135] X. Zhai, Z. Xu, Q. Cui, Y. Zhu, H. Yang, and Y. M. Blanter, Electrically Controllable van der Waals Antiferromagnetic Spin Valve, *Phys. Rev. Appl.* **16**, 014032 (2021).
- [136] X. Wu, H. Meng, H. Zhang, and N. Xu, Magnetoresistance effect realized in current-in-plane van der Waals spin valve structure by electrically switchable magnetization, *New J. Phys.* **23**, 103007 (2021).
- [137] Calculating the DOS from DFT would require a dense sampling of the Brillouin zone and a huge number of *k* points, which is computationally demanding, given also the large number of atoms in the encapsulated TLG supercells. We circumvent this problem by employing the model Hamiltonian, which very accurately reproduces the low-energy dispersions. For the model DOS calculations, we employ a *k*-point grid of 5000 × 5000 in the vicinity ( $\pm 0.1 \text{ \AA}^{-1}$ ) of the *K* point.
- [138] A. L. Rakhmanov, A. V. Rozhkov, A. O. Sboychakov, and F. Nori, Instabilities of the AA-Stacked Graphene Bilayer, *Phys. Rev. Lett.* **109**, 206801 (2012).
- [139] A. V. Rozhkov, A. O. Sboychakov, A. L. Rakhmanov, and F. Nori, Electronic properties of graphene-based bilayer systems, *Phys. Rep.* **648**, 1 (2016).